Application of Cutting-Edge 3D Seismic Attribute Technology to the Assessment of Geological Reservoirs for CO_2 Sequestration

Type of Report: Progress

Frequency of Report: Quarterly

Reporting Period: October 1, 2009 – December 31, 2009

DOE Award Number: DE-FG26-06NT42734 [University Coal Research]
(UH budget G091836)

Submitting Organizations: Department of Earth and Atmospheric Sciences
Reservoir Quantification Lab
University of Houston
Houston, Texas 77204-5505

Preparers: Prof. Christopher Liner - P.I.
Dr. Jianjun (June) Zeng
Dr. Po Geng (coordinator for this report)
Heather King
Jintan Li
Bryan Flinn
Shannon LeBlanc
Phone: 713-743-9119
Fax: 713-748-7906

CONTENTS

Executive Summary

This report presents major advances in progress made through the report period from October 1 to December 31 of 2009 for the Dickman Field CO_2 sequestration characterization project.

The geometry and property of Mississippian (Miss) carbonate and basal Pennsylvanian (Penn) Lower Cherokee sandstone reservoirs are controlled by sedimentary facies in different deposition environments, including paleo-topography, syn-depositional structural activities, and post-depositional faulting/fracturing/deformation.

A brief summary on the local Pre- and Post Miss geological events and their effects on reservoir conductivity was presented In Q3 2009 report. This report includes details on the post-Miss structure activities that affected the fracturing and deformation of the Miss and Penn strata, in the geology progress section. The data analysis provides basic information on recognizing the fracture system and the properties to set constraints on reservoir property modeling.

Initial progress made in the time-lapse seismic (4D) method is discussed in this report.

The focus of flow simulation was on CO_2 storage safety. First, three CO_2 trapping efficiency indices were defined to measure the safety of CO_2 sequestration. A series of numerical simulations were performed to determine CO_2 sequestration trapping efficiency under different CO_2 injection conditions. Additional flow simulation work included redoing the history matching simulation using the updated reservoir model and conducting an initial study on the possibility of applying CO_2 water alternatng gas (WAG) technology to Dickman field.

Activities in Quarter

Geology and Geophysics

Geology

The progress in Geology includes an extension of the deep saline aquifer to the entire middle Mississippian (Miss) strata at the Miss/ Devonian boundary, and a detailed discussion of Post-Miss structural history.

Extension of the Deep Saline aquifer for the CO2 injection simulation.
Figure 1 shows the regional stratigraphic column (left) of the Penn and Miss strata, and the corresponding local lithologic column (right) of the target strata for the flow simulation. Blue callout boxes identify the target reservoirs for history-matching simulation and the extended deep saline aquifer for CO2 injection simulation.

The lower boundary of the deep saline aquifer for CO2 injection simulation is set at the B Horizon determined from seismic as corresponding to the Miss-Devonian contact. In the survey area to the southwest of the Central Kansan Uplift, however, the Devonian and Silurian are mostly missing or undifferentiated. From well data, the B Horizon roughly corresponds to the top of the Viola limestone (middle Ordovician) as seen from three wells that fully penetrated the Miss. The Lower Kinderhookian is missing in the studied area as shown in the regional stratigraphic section (Figure 1, left). Extending the saline aquifer and simulation model to the base of the Miss (top Viola) added the entire Upper Kinderhookian strata (120-130 ft). The thickness of the modeled deep-saline aquifer therefore has changed from about 70 ft to over 200 ft. The porosity and permeability data used in CO2 injection simulation were extrapolated from the three wells penetrating the target saline aquifer.

Re-construction of Post-Mississippian structural history
Geometry and properties of Penn sandstones and Miss carbonates in the Dickman area are defined by: 1) sedimentary facies in various deposition environments controlled by paleo-geography and syn-depositional structural activities, and 2) post-depositional faulting/fracturing or deformation. A brief summary on the local pre- and post- Miss geological events and their reservoir effect was presented in the Q3 2009 report. The following discussions focus on the post-Miss structure activities that affected the deformation and fracturing of the Miss and basal Penn strata. The analysis provides basic information related to geometry and style and of the 3D fracture system in the Dickman area.

For structural reconstruction, Figure 1 serves as the relative geological age reference and Figure 2 gives an outline of the post-Miss structural framework from global to local scale. The major post-Miss uplift event marked by the Miss unconformity was a result of continental collision. Basement faulting to the south west of the Central Kansan Uplift provides secondary structural control. The basement faulting has been active from

Cambrian to the present day, as revealed by basement and the present day drainage system.

Significant differences in local structure patterns exist between the younger Penn and older Miss strata, as shown by formation top gridded depth maps of the Ft. Scott Limestone and Miss unconformity (Figure 3). The Ft. Scott structure is oriented primarily NE-SW, while the Miss exhibits both NE and NW trending features.

The top of the Ft. Scott Limestone (Figure 3, left) shows a NE-plunging fold-like structure (blue arrow). The south end of this structure, overlying paleo-lows of the Miss unconformity, formed a hydrocarbon closure (35 ft) producing from the Lower Cherokee Sandstone. The north end of this structure, is a drag fold on the foot-wall side of a fault (marked purple) as seen in the seismic profile of Figure 4. The NE boundary fault offsets the Ft. Scott significantly, suggesting that its latest faulting activity was post-Penn. It is hard to see changes in strata thicknesses across this NE fault, for either Penn or Miss Miss from the seismic profile. Whether or not this fault is syn-depositional (during Penn time), cannot be determined due to lack of well data on the hanging wall (NW) side.

Unlike the Ft. Scott, the older Miss unconformity shows structural complexity, including isolated lows separating isolated highs, very likely controlled by both NE and NW oriented structures. As shown by cross sections from top Ft. Scott to the Miss unconformity (Figure 5), the thickness and lithology of the Penn strata is controlled by Miss paleo-topography. The well cross section in Figure 5 is perpendicular to the NE structure axis across the NE boundary fault, with two topographic highs and one low on the Miss. The Penn section thickness is greater where the Miss has a topographic low (Elmore 2, filled mainly by the coarse-grained Lower Cherokee Sandstone) and becomes thinner on topographic highs toward the Humphrey 4-18 and Sidebottom 4. As the Penn section thins, the Lower Cherokee sandstone also thins and is ultimately missing in Humphrey 4-18 area.

From top-down in the cross section, there is no significant lateral thickness variation between the Ft. Scott Limestone and Base Penn Limestone tops (Figure 5). The thickness variation occurs mainly in the lower Penn section, between the basal Penn Limestone and the Miss unconformity. This indicates a stronger topographic-control on the deposition mainly during the early Penn, including the Cherokee Sandstone and the basal Penn limestone. This topographic control is regional as shown by the stratigraphic column in Figure 1, in which the basal Penn Limestone and the Cherokee Sandstone are laterally interwoven on top of the Miss unconformity. This interpretation is also supported by well cross sections parallel to the structure axis.

The thickness isopach of Penn strata reveals the spatial distribution of the Miss paleotopography (Figure 6). The Ft. Scott to Miss unconformity isopach indicates that deposition of the Penn strata mold-casted the Miss paleotopography. The Penn section thins coincident with Miss highs, and thickens at Miss lows. As shown in Figure 5, the sediment infill was mostly the coarse Lower Cherokee Sandstone on the channel bend cut into the Miss unconformity. Our Miss paleotopography interpretation is also supported

by the seismic Miss time structure map shown in Figure 7. With better horizontal continuity than sparse formation tops, the seismic clearly reveals the Lower Cherokee channel bend.

The development of this paleotopography was related to a pre-Penn structural framework that had a stronger contribution from NW-oriented structures. Seismic profiles perpendicular to these possible NW structures from the spice volume better resolve the spatial pattern in older strata (Figure 8). Most of the NW-oriented discontinuities cut through only the Gilmore City and Miss unconformities. The thickness of Miss strata shows no significant variation, suggesting that structural movements are probably post-Miss.

The thickness of the Penn strata, however, varies significantly across some NW faults. For instance, the Penn thickness in the down thrown side of the red fault (Figure 8) is over 152 feet at the Tilley 4 well, but only 96 ft on the up-thrown side the wells (Tilley1b and 2). Since well top and lithology data do not show a systemat shift of lower Penn lithofacies with stratigraphic thinning, faulting was likely pre-depositional (early Penn) rather than syn-depositional (growth faulting). This further indicates that Miss paleotopography was the major control on lower Penn thickness and lithology variation.

The Miss paleotopographic highs were separated by NW structures. As seen in Figure 6, the Miss high around the Dickman 3a well is between the two NW faults. The topography seen on the Miss unconformity at Dickman is common in some present day carbonate plateaus, where the dissolution of exposed carbonate strata is much stronger along fault and fractured zones forming karst sinkholes or caves. When caves collapse, residual hills are formed. Well data in the Dickman Field support karsting as the origin of the observed Miss unconformity topography. Salem Limestone, the youngest Miss carbonate below the unconformity, shows significant thickness variation with top Miss topography. It is generally much thicker on the topographic highs (about 33-41 ft at Dickman 1 and 3a), and thinner at topographic lows (10-14 ft at Dickman A2 and Tilley 1). This is especially true within the Lower Cherokee Sandstone channel (Phelps 1a and Staiwalt 1). These topographic highs with thicker Salem Limestone were the erosional residual hills on the Miss karst topography, while in the lows are due to preferred dissolution along NW and NE fractured zones.

In summary, interpretation of several major post-Miss events were supported by Dickman well and seismic data.
1) Tectonic movement after the deposition of Miss carbonate strata resulted in the regional uplift associated with NE and NW faults and fracturing. Structurally controlled karst topography developed on the exposed Miss surface.
2) This karst topography controled deposition of early Penn strata, evidenced by interwoven basal Penn limestone and sandstone units with varying thickness.
3) The paleo-geography control on the Penn deposition became less important during the late Penn, as shown by near constant thickness of the Cherokee (coal/sand/shale) and Ft. Scott (limestone) complexes.

4) Faulting along the NW direction became less active during Penn time, and did not affect deposition of upper Penn strata.
5) The latest faulting episode along the NE-direction was post-Penn, resulting in a NE-oriented shallow fold structure. This developed a hydrocarbon closure in the Penn Cherokee Group to the southwest, and a NE boundary fault as a major hydrocarbon seal in the Dickman, Sargent and Humphrey areas.

The style and timing of the structural framework can be used to set constraints for reservoir property modeling. The fracture framework shown in Figure 9 was made from three sources of information. Dark green features are based on un-gridded seismic fault interpretation and verified using well data. Light blue are based on the gridded seismic fault interpretation only. Red features are discontinuities extracted from the structure-smoothed, variance-enhanced seismic volume. In the 3D property modeling, constraints along sealing NE faults/fractures were set as the least preferred orientation of lateral continuity, and those along open NW faults/fractures were set as most preferred orientation of lateral continuity. For the sealing condition evaluation, the youngest NE boundary fault was a sealing fault for the hydrocarbon traps, unlikely to be a leaching conduit. The NW faults/fractures are unlikely to be leaking conduits on the Ft. Scott seal.

Geophysics

The effort was made in this quarter to simulate time-lapse seismic (4D) to monitor the state of the reservoir, due to changes of fluid properties at periodic times. The change of fluid properties such as fluid saturation, pressure, temperature, porosity etc. will have impact on the seismic responses. Hence, by differencing the seismic responses at varied times the reservoir characteristics can be analyzed.

Methods

The link between rock physics and seismic modeling is realized by first calculating the seismic velocity and density for the saturated rock at each simulation cell, then calculating seismic reflection coefficients from impedance contrast. Given an input wavelet, seismograms can be generated by some modeling method. A few good candidates can be the modest convolution model, ray-tracing, Eikonal solver, or two-way wave modeling by finite difference.

The current CO_2 flow simulation calculations utilize the Computer Modeling Group (CMG) generalized equation of state compositional simulator (GEM) which can be used in CO_2 enhanced oil recovery and CO_2 storage. I used all the requisite parameters from this simulation output into the fluid saturation Gassmann's theory.

In this case, considering the simulation output as a three-dimensional volume with the size of **M** x **N** x **L** in x, y, z directions, as illustrated in Figure 10. We'd like define that the seismic bin size is the same as that of the simulation cell, which may need more discussion and choices of parameters regarding the seismic resolution. In each bin, we generate the seismic synthetics as a summed trace. For each grid within the seismic bin,

we read in all the parameters from the simulation output to calculate impedance, and then calculate the reflection coefficients in this bin.

The calculations of different bulk modulus of the reservoir are needed as input for the Gassmann's equation. They include: bulk modulus for the porous dry rock ($\mathbf{K_{dry}}$), bulk modulus for the solid mineral ($\mathbf{K_{min}}$), bulk modulus for the fluid ($\mathbf{K_{fluid}}$). The details are discussed in the following steps.

Temperature and Pressure Regime

Before calculating the different properties of the saturated rock, the temperature and pressure need to be corrected with depth. Since the bottom-hole temperatures are recorded during logging of the borehole and commonly are not at equilibrium with formation temperature (Carr, Merriam and Bartley, 2005), the temperature (unit: Franheit) for Mississippian is a function of depth:

T=0.0131(depth)+55 (1)

For the deep saline aquifer (Arbuckle group):

T=0.0142(depth)+55 (2)

The pressure gradient is 0.476 psi/ft for both the Mississippian and the saline aquifer.

P=0.476(depth)

Calculation of K_{min}

The lithology of the Mississippian unconformity is composed predominately of dolomite and calcite. So the frame mineral bulk modulus can be estimated from the bulk modulus Kmin can be estimated from the Voigt-Reuss-Hill (VRH) averaging (Hill, 1952) constitutes as follows:

$$|K_{min} = \frac{1}{2}([V_{dolo}K_{dolo} + V_{cal}K_{cal}] + [\frac{V_{dolo}}{K_{dolo}} + \frac{V_{cal}}{K_{cal}}])$$

where the dolomite takes about 70% of the mineral and calcite takes about 30% of the volume. So the density can be calculated as:

$$\rho_{min} = V_{dolo}\rho_{dolo} + V_{cal}\rho_{cal}$$

(here Vdolo=0.7, and Vcal=0.3)

The densities ρ_{dolo} and ρ_{cal} can be found in the text book of (Mavko, Mukerji and Dvorkin).

$K_{dolomite} = 83(Gpa),\ K_{calcite} = 76.8(Gpa);\ \rho_{dolomite} = 2.87g/cm^3,\ \rho_{calcite} =$ 2.71g/cm3

Calculation of K_{fluid}

The fluid content we consider here are brine, oil and CO_2. For the current stage, the solubility of CO2 into water or oil is neglected. We consider them as three independent phases without any interference with each other.

ρ_{sat} satisfies the relationship between the fluid density ρ_{fluid}, grain density of the rock matrix ρ_{min} and porosity ϕ:

$$\rho_{fluid} = S_w\rho_w + S_o\rho_{oil} + S_{co_2}\rho_{co_2}$$

$$\rho_{sat} = (1-\phi)\rho_{min} + \phi\rho_{fluid}$$

The total bulk modulus for the fluid by Wood's equation is:

$$\frac{1}{K_{fluid}} = \frac{S_w}{K_w} + \frac{S_{oil}}{K_{oil}} + \frac{S_{co2}}{K_{co2}}$$

Calculation of K_{oil}

The bulk modulus for the oil is expressed as:

$K_{oil} = \rho_{oil}V_{oil}^2/1000$

ρ_{oil} can be obtained by a series of equations which relate to the fluid gravity (G), reservoir temperature (T) and fluid pressure (P) as below (Batzel and Wang):

$$\rho_{oil} = \rho_G + (0.00277 - P - 1.71\times10^{-7}P^3)(\rho_G - 1.15)^2 + 3.49\times10^{-4}P$$

$$\rho_G = (\rho_o + 0.002GR_G)/B_o$$

$$\rho_o = \frac{141.5}{API + 131.5}$$

$$R_G = 3.03G(Pe^{0.02878API - 0.00377T}) \times 1.205$$

$$B_o = 0.972 + 0.00038 \times [2.4R_G\sqrt{\frac{G}{\rho_o}} + T + 17.8]^{1.175}$$

The velocity of oil can be calculated by (Batzel and Wang):

$$V_{oil} = 2096(\frac{\rho'}{2.6-\rho'})^{0.5} - 3.7T + 4.64P + 0.015 \times [4.12\sqrt{\frac{1.08}{\rho'-1}}]TP$$

$$\rho' = \frac{\rho_o}{B_o(1+0.001R_G)}$$

Calculation of K_{brine}

Bulk modulus for the brine can be attained by:

$$K_{brine} = \rho_{brine} \times V_{brine} \times 10^{-6}$$

the density of brine is calculated by (Batze and Wang):

$$\rho_{brine} = \rho_w + 0.0668S + 0.44S^2 + 10^{-6}S[300P - 2400PS + T(80 + 3T - 3300S - 13P + 47PS)]$$

where T is temperature and P is pressure

The water density is also dependant on T and P:

$$\rho_w = 1 + 10^{-6}(-80T - 3.3T^2 + 0.00175T^3 + 489P - 2TP + 0.016T^2P - 1.3 \times 10^{-5}T^3P - 0.333P^2 - 0.002TP^2)$$

For the P-wave velocity of brine, it uses the following equation:

$$V_{brine} = V_m + S(1170 - 9.6T + 0.055T^2 - 8.5 \times 10^{-3} + 2.6P - 0.0029TP - 0.0476P^2)$$

$$+S^{1.5}(780 - 10P + 0.16P^2) - 1820S$$

here Vm is the velocity in pure water, which can be estimated from the following equation: (Batzel and Wang)

$$V_w = \sum_{i=1}^{5}\sum_{j=1}^{4} \omega_{ij} T^{i-1} P^{j-1}$$

the weight coefficients ω_{ij} is given in the table. The salinity in the Dickman field is 45,000ppm.

Table 1. Coefficients for water velocity computation (from Batzle and Wang, 1992)

w_{11} = 1402.85	w_{13} = 3.437×10^{-3}
w_{21} = 4.871	w_{23} = 1.739×10^{-4}
w_{31} = -0.04783	w_{33} = -2.135×10^{-6}
w_{41} = 1.487×10^{-4}	w_{43} = -1.455×10^{-8}
w_{51} = -2.197×10^{-7}	w_{53} = 5.23×10^{-11}
w_{12} = 1.524	w_{14} = -1.197×10^{-5}
w_{22} = -0.0111	w_{24} = -1.628×10^{-6}
w_{32} = 2.747×10^{-4}	w_{34} = 1.237×10^{-8}
w_{42} = -6.503×10^{-7}	w_{44} = 1.327×10^{-10}
w_{52} = 7.987×10^{-10}	w_{54} = -4.614×10^{-13}

Table . Coefficients for water velocity computation (Batzel and Wang)}

Calculation of K_{CO2}

CO_2 properties are calculated from the online source from Kansas geological survey given a certain temperature and pressure.
(http://www.kgs.ku.edu/Magellan/Midcarb/co2_prop.html)

In this case, Mississippian unconformity has an average measured depth of 4424 ft, so the reservoir temperature and pressure should be:

T=0.0131*4424 + 55 = 113 ^{o}F

and

P = 0.476*4424 = 2106 psi

bring these into the online CO_2 properties calculator, we obtain:
$\rho_{CO2} = 46.54 lbs/cu - ft$ and $KCO2 = 1/0.3248$ mpa

Reservoir Temperature	110	Degrees F
Reservoir Pressure	2100	psia
Update		
Density	46.54	lbs/cu-ft
Compressibility Factor	.3248	
Sonic Velocity	1213.7	ft/sec
Viscosity	.06157	cp
Volume Factor	.4438	bbl/MCF
Phase	Dense Vapor	

Chart 2. Co2 properties calculator

Calculation of K_{dry}

Kdry can be obtained by rewriting the Gassmann's equation:

$$K_{dry} = \frac{K_{sat}\left(\frac{\phi K_{min}}{K_{fluid}} + 1 - \phi\right) - K_{min}}{\frac{\phi K_{min}}{K_{fluid}} + \frac{K_{sat}}{K_{min}} - 1 - \phi}$$

In the Gassmann's theory, in terms of saturated rock moduli, the following assumption is assumed:

$$\mu_{sat} = \mu_{dry}$$

In the Dickman field properties, we have one shear wave sonic log for the well Elmore 3. But we are not certain if the shear sonic log is measured or calculated, but it's used for the current Vs calculation. Elmore 3 doesn't have a density log, so I use the density log from a nearby well for the density.

the initial estimate can be calculated by:

$K_{sat} = \rho(Vp^2 - \frac{4}{3}Vs^2)$

the shear modulus can be calculated from the shear wave sonic log:

$$\mu_{sat} = \rho V s^2$$

Calculation of K_{sat}

Bring K_{min}, K_{dry}, K_{fluid} into Gassmann's equation to get K_{sat}:

$$K_{sat} = K_{dry} + \frac{(1 - \frac{K_{dry}}{K_{min}})^2}{\frac{\phi}{K_{fluid}} + \frac{1-\phi}{K_{min}} - \frac{K_{dry}}{{K_{min}}^2}}$$

Calculation of Reflection Coefficient

First, the velocity for the saturated rock can be estimated from the following:
the initial estimate can be calculated by:

$$V_{sat} = \sqrt{\frac{K_{sat} + \frac{4}{3}\mu_{sat}}{\rho_{sat}}}$$

Then calculate impedance by:

$$Imp = \rho_{sat} V_{sat}$$

so the reflection coefficient can be calculated by:
For i=1,...N-1

$$R(i) = \frac{Z_{i+1} - Z_i}{Z_{i+1} + Z_i}$$

Work Flow

Here we show a 2D case as an example. As illustrated in Figure 11, for the jth simulation column within the seismic bin (j=1,...M), the time-lapse seismic modeling works as follows:
1) read the i^{th} simulation grid (i=1,.., N), which contains the information of porosity, saturated density, pressure, water gas oil saturations, etc.

- compute bulk modulus for different fluids (oil, CO_2, brine)
  a) bulk modulus for oil
  b) bulk modulus for brine
  c) bulk modulus for CO_2

- compute the initial bulk modulus for saturated rock
- calculate the bulk modulus for the porous rock frame Kdry with the initial Ksat
- update Ksat using Gassmann's equation with fluid substitution
- calculate the velocity for the saturated rock by:
- compute impedance with saturated density and velocity in this simulation grid

$$Z_i = V_{sat}\rho_{sat}$$

2) read the next simulation grid, and repeat the steps above until all the impedance values have been calculated in this bin
3) calculate the reflection coefficients in this bin.
4) read the next bin, j=j+1, repeat the steps above.

The final output will be considered as a poststack 3D seismic cube. The interpretation can be done on the new volume to compare the reservoir changes at different time.

Results

We gave a framework and work flow of how this seismic lapse modeling works. In the current stage, we would like to show a preliminary result of the reflection coefficients calculation between Ft.scott and Mississippian unconformity. The lateral distribution of Mississippian is primarily controlled by depositional facies in carbonate build-ups (Carr et. al., 1999), which is composed of Lower Cherokee sandstone and the rest carbonate is predominantly of limestone. Due to this porous structure, for the composition with more fluid content, we employed Gassmann's therory for calculating the density and velocity for the saturated rock. Considering the seismic resolution, the thickness of the overlying reservoir has to be at least one quarter of wavelength, so we chose the thickness threshold of 25ft. If the thickness is less than 25ft, the lithology is considered as sandstone, otherwise as limestone. The velocity of Ft.scott sandstone is obtained from the six wells with sonic curves gridded throughout the whole survey, and so is density.
The fluid content we consider here is only brine and CO_2, the oil can be added later. The CO_2 saturation at different depth is directly exported from the CMG flow simulation output. The average porosity is around 20 percent for the Miss unconformity, shown as in Figure 12.

The code was written in Matlab and will be converted into C to be added into the Seismic Unix. For a given well, when the temperature changes, the CO_2 saturation changes. Keeping all other parameters fixed with time, the reflection coefficients also change with time as shown in Figure 13. Figure 14 shows another graph which porosity changes with time while other parameters remain fixed, the CO_2 saturation is around 14% in this case.

Flow Simulation

The flow simulation work in this quarter was preceded in three parts: CO_2 sequestration in deep saline aquifer, an initial study on CO_2 water alternating gas (WAG) technology, and history matching on the Dickman oil reservoir.

CO_2 sequestration in deep saline aquifer

The previous flow simulation study was focused on the establishment of the simulation model (properties and grid) and the grid convergence study. The solubility of CO_2 in brine was used as an indicator for the convergence study. The numerical result indicated that for the current aquifer model, to insure a simulation error under 20%, a grid cell size less than 250 by 250 feet was required. If the grid size was less than 125 feet by 125 feet,

a 5% solution error could be expected. Local grid refinement around the injecting well can increase the solution accuracy effectively.

Some significant changes were made to the previous aquifer model with the new and re-interpreted log and seismic data. Now the aquifer model has been simplified as one consisting of the following five geological units:

1. Ft. Scott Limestone
2. Cherokee Group
3. Lower Cherokee Sandstone
4. Mississippian Carbonate
5. Lower Mississippian Carbonate

A twenty-four layer simulation model as shown in Figure 15 was constructed for CO_2 sequestration simulation. The relationship of geological layers and simulation layers are as follows:

Simulation Layer	**Geological Layer**	**Lithology**	**K_v/K_h**
1-2	Ford Scott	Limestone	0.7
3-5	Cherokee Group	Sandstone	0.5
6-7	lower Cherokee	Sand Stone	0.5
8-12	Mississippian	Carbonate	0.7
13-24	Lower Mississippian	Carbonate	0.7

The new and updated permeability and porosity data obtained from well log analysis were used in the simulation model. Based on the core testing results, we assumed the ratio of the vertical permeability vs. horizontal permeability (K_v/K_h) as 0.7 for generalized carbonate and limestone and as 0.5 for sandstone.

Dickman filed CO_2 storage safety is a major issue addressed in this quarter. As indicated by Nghiem et al. (2009), the CO_2 injected into aquifers is trapped by four different mechanisms:

1. Mineral Trapping
2. Residual Gas Trapping,
3. Solubility Trapping, and
4. Structural Trapping,

The mineral trapping mechanism is the safest, most permanent solution. The dissolved CO_2 in a saline aquifer will decompose into H^+ and HCO_3^- which in turn react with the minerals in place. Such chemical reaction will induce precipitation of carbonate minerals such as calcite, dolomite and siderite. The process of CO_2 precipitation is extremely slow and minimal for the first thousand years after CO_2 injection.

Residual gas trapping is a process that traps CO_2 as an immobile gas in the porous media, and is considered nearly as permanent/safe as mineral trapping. The classical Land's residual trapping model is used in the CMG GEM simulator to this process. Figure 16 shows a typical gas relative permeability curve. When the gas (CO_2) saturation increases, the gas relative permeability follows the drainage curve k_{rg}^{d} (black curve in Figure 16). If at the saturation S_{gi}^{*} on the drainage curve, the gas saturation reverses its course and decreases, the gas relative permeability follows the imbibitions curve k_{rg}^{i}(red curve). The typical value of $S_{gt,max}$ is 0.3 to 0.4. We assumed $S_{gt,max} = 0.4$ in this study.

CO_2 gas is highly soluble in brine. The only safety risk of the dissolved CO_2 gas is that the brine and dissolved CO_2 may migrate to the surface. According to Timothy et al (2008), the underground water migration speed around Dickman field is only about 40 feet per million years, which eliminates the possibility that any dissolved CO2 gas will be migrated to the surface. Thus the solubility trapping is also considered as a safe CO_2 trapping mechanism in this case. In CMG GEM simulator, CO_2 solubility in brine is calculated by solving the fugacity equation of

$$f_{CO_2,aq} = f_{CO_2,g}$$

where $f_{CO_2,aq}$ and $f_{CO_2,g}$ are the fugacity of CO2 in aqueous phase and gas phase, respectively. The gas fugacity $f_{CO_2,g}$ is calculated by using a cubic equation of state (Peng-Roberson equation in the most cases) and the aqueous phase fugacity $f_{CO_2,aq}$ is calculated by using Henry's law

$$f_{CO_2,aq} = H_{CO_2,aq} \times Y_{CO_2,aq}$$

where $H_{CO_2,aq}$ is Henry constant which is a function of temperature, pressure and salinity and $Y_{CO_2,aq}$ is the mole fraction of CO_2 in brine.

Free CO_2 gas trapped in a geological structure represents a real safety threat. This portion of CO_2 can migrate to the surface through faults, fractures, a failed cap rock or corroded well pipe. Han et al. (2009) have shown that theoretical wellpipe corrosion rates are on the order of 30-60 mm/yr (80 F and 84 Bar), although experiments indicate a much slower corrosion rate on the order of 1-2 mm/yr. A feasible way of improving CO_2 storage safety is to accelerate the process of residual gas trapping and solubility trapping.

The following trapping indices were defined to give a convenient measurement on the effectiveness of a CO_2 injection process:

$$\text{Residual Gas Trapping Index RTI(t)} = \frac{\text{Total amount of } CO_2 \text{ trapped as residual gas at time t}}{\text{Total amount of } CO_2 \text{ Injected at time t}}$$

$$\text{Solubilty Trapping Index STI(t)} = \frac{\text{Total amount of } CO_2 \text{ dissolved in brine at time t}}{\text{Total amount of } CO_2 \text{ Injected at time t}}$$

$$\text{Trapping Efficiency Index TEI(t)} = \text{RTI(t)} + \text{STI(t)}$$

In this quarter, three trapping mechanisms, structural, solubility and gas residual trapping were included in flow simulations. Trapping efficiencies were calculated for two different CO_2 injection scenarios: CO_2 injection only and CO_2 injection with water were calculated. The effectiveness of using a horizontal injection well was also studied. Figure 17 shows the arrangement of a vertical and a horizontal injector for CO_2 injection only test cases. Both injector wells are perforated in the bottom simulation layer. CO_2 injection rate was set to $6.67 \times 10^6 ft^3/day$ or 346 ton/day with the maximum pressure not exceeding 5000 psia. CO_2 injection is done for first 25 years, and the injector is shut in thereafter and the fate of CO_2 is modeled for the next 225 years. Figure 18 compares the amount CO_2 trapped by the different trapping mechanisms for the vertical injection well and horizontal injection well. For the CO_2 only injection, the total mass of CO_2 trapped by solubility and residual gas trapping is only about 56% at the time of 250 years. Comparing to the vertical well, the horizontal well increases the well perforation length from 25 feet to 2000 feet but it only increases the total mass of CO_2 dissolved in brine water from 13% to 17.4% and TEI from 53% to 56%.

The reason of the low CO_2 trapping efficiency is the accumulation of high concentration CO_2 around the well bore hole. An effective way of reducing CO_2 concentration around the borehole is to inject water above the perforation during CO_2 injection. Figure 19 shows the vertical and horizontal injection well simulation setup for CO_2 injection with brine. The bottom perforations are for CO_2 injection and the upper perforations are for water injection. CO_2 daily injection rate is still 6.67 million stb/day or 346 ton/day. The maximum water injection rate per day allowed for the vertical well under 5000 psia is 6500 bbl/day. So we set the water injection rate for both vertical well and horizontal well as 6500 bbl/day. Figure 20 is the comparison of the amount of CO_2 trapped by different mechanisms for the entire simulation period. In the case of CO_2 injection with water, using horizontal injection well can increase CO_2 trapping efficiency significantly. A summary of the simulation results for the simulation grid size of $31 \times 33 \times 24$ is given in Table 1. As shown in Table 1, comparing with the vertical injection well, the horizontal injection well can increase CO_2 trapping efficiency from 58.1% to 94.2%. Another benefit of using horizontal injection wells is that it can reduce the maximum bottom hole pressure significantly. As shown in Table 3, the horizontal injection well can reduce the maximum bottom hole pressure is 2367 psia (horizontal) compared to 5000 psia (vertical).

Initial Investigation on WAG

CO_2 enhanced oil recovery is an important part of CO_2 sequestration. It can increase the oil production and meantime leave part of the injected CO_2 underground. Water Alternating Gas (WAG) is the most promising way of CO_2 enhanced oil recovery. In this quarter, we did some studies to understand the possibility of performing CO_2 WAG at Dickman field. The process of water alternating gas (WAG) is a combination of two traditional oil recovery techniques: water flooding and gas flooding. During a flooding event, the oil recovery rate is determined by three factors:

$$R_{oil} = E_m \times E_v \times E_{area}$$

where R_{oil} is the oil recovery rate, E_v is the vertical sweep displacement efficiency, E_{area} is the area sweep displacement efficiency and E_m is the microscopic displacement efficiency.

There are two types of oil displacement mechanisms: miscible displacement and immiscible displacement which is separated by a minimum miscible pressure (MMP). When the injection pressure is greater than MMP, the injected gas becomes miscible with oil and a miscible displacement process is performed. Otherwise an immiscible displacement is performed. There are several different definitions to determine the minimum miscible pressure (Enick et al., 1988). CO_2 MMP in Figure 21 is determined by a sharp change in slope of the recovery vs. pressure curve. Figure 22 is Correlation of predicting CO_2 MMP for oils with different heavy C_5+ hydrocarbon components (Helm et al., 1974).

When performing a miscible displacement, the residual oil saturation will go toward zero in the gas flooded areas. Even with an immiscible displacement, the remaining oil saturation after gas flooding is normally lower than after water flooding. The experimental result shown in Figure 23 was given by (Helm et al., 1974). The experimental sample consists of a series of the consolidated sandstone core samples with the total length of 96 feet. The sample was filled with brine water and 38 API oil. The experimental pressure is 900 psi. This is below CO_2 minimum miscible pressure at the experimental temperature of 75°F, so CO_2 flooding is immiscible. As shown in Figure 23, the residual oil saturation is about 30% after water flooding and is less than 15% after immiscible CO_2 flooding. The gas always has better microscopic displacement efficiency E_m than water.

The area displacement efficiency E_{area} is strongly influenced by the mobility of the fluids. The mobility ratio M can be described as

$$M = \frac{k_{rg}/\mu_g}{k_{ro}/\mu_o}$$

where k_{rg} and k_{ro} are the relative permeability and μ_g and μ_o are the viscosity of gas and oil, respectively. Figure 24 shows a correlation of areal sweep efficiency as a function of the water-oil mobility ratio for five-spot patterns. As the mobility ratio increases, the area sweep efficiency E_{area} will decrease. The vertical displacement efficiency for a gas flooding process is determined by the gravitational force, viscosity and reservoir heterogeneity. In general, a smaller mobility ratio will give better vertical displacement efficiency.

Because the gas viscosity is much smaller the oil viscosity, the mobility ratio is usually very large for a gas only flooding processing. The viscosity of the gas can be increased by injecting water with gas. It is not practical to inject different fluids in a well at same time. Figure 25 shows a general procedure of enhanced oil recovery procedure used by the oil industry. The different fluids are injected consequently in the different slugs. By following the same procedure, the gas and water should be injected alternately. This process is referred as WAG (water altering gas).

Actually, CO_2 in a supercritical state (temperature > 87.8 ^oF and pressure > 1076 psi) is miscible to light oil with API > 35. The average pressure of Dickman field is 2066 psia and the temperature is 113 ^oF and API oil density of Dickman field is 37. So there would be miscible displacement of oil if a CO_2 flooding were performed in the Dickman field.

Dickman Field History Matching Simulation

The role of history matching is to test and improve a reservoir model. The reservoir property data, formation structural data and production data collected from different sources will be validated or calibrated through the history matching process. The history match result will be used to improve the existing reservoir model. Because some crucial data including well pressure, perforation and gas production data are missing at Dickman, history matching is a difficult task. In this quarter, the geological team updated the reservoir model based on all available information and feedback from the previous history matching study. We conducted history matching simulation again using the updated model and give a progress report here.

Dickman Field was discovered and put into production in 1962. From Hilpman et al. (1964), Timothy et al. (1982), and Osif (1957), we have the following data for Dickman field

Acreage = 240 acres
Net Pay Zone Thickness = 7 feet
Average depth = 4424 feet in MD
Oil API gravity γ_o = 37 API (0.84 g/cm^3)
The reservoir Temperature = 113 ^oF
The reservoir average pressure = 2066 psia
TDS (Total Dissolved Solid) salinity = 45,000 ppm
The aquifer water density $\gamma_w = 1.03\ g/cm^3$ at reservoir condition
The reservoir water compressibility $C_w = 3 \times 10^{-6}\ 1/psi$ at reservoir condition
The water oil contact depth = 4581 feet in MD (from well log data)

PVT lab fluid properties are not available at this time. We have to use PVT data generated by PVT correlations. The majority part of Dickman field pay zone is located in Mississippian carbonate zone. Normally, a large oil-water transition zone is expected in a carbonate zone. The well log analysis also indicated that there exists a large water-oil transition zone in Dickman. A good discussion about the capillary transition zone in carbonate reservoir was given by Masalmeh et al (2005). The capillary curves defined in Figure 26 were used to model the water-oil transition zone in the history matching simulation. Table 3 is PVT data generated by using Lasater's black oil correlation (McCain, 1991). Figure 27 shows the water and oil relative permeability curves and the gas and total liquid relative permeability curves used in the simulation. Dickman field is an aquifer water drive reservoir. Carter-Tracy aquifer boundaries were used to set aquifer influx conditions.

The history data of total 22 production wells around Dickman field were provided by Grand Mesa Production Company. Figure 28 shows the simulation grid for the history matching simulation and 13 production wells listed in Table 4 belong to Dickman field. At the end of 2008, the total oil produced from 13 production wells is 1.52 million barrels. By setting a proper oil-water contact depth and transition zone, we can easily match the total oil production. We are working to match the oil production rate and water cut for each production wells.

Work Plan for the Next Quarter

As the principal investigator, C. Liner will be scoping out the final project report and looking further into the mapping of fracture trends with Spice, he will also be submitting an abstract for an invited lecture on CO_2 sequestration at the Offshore Technology Conference in May.

Geology and Geophysics

For the next quarter, we will continue to work on

1. Refining the fracture framework to set more constraints for the property grid, based on ANT-extraction from the spice volume,
2. Re-adjusting the 3D geometry and property grids to provide an input data set for a site-specific CO_2 injection simulation model, based on the history-matching test results, and
3. Continue working on 4D to generate 3D seismic volumes for different geophysical attributes analysis.

In addition, an abstract will be submitted to the 2010 CO_2 annual meeting. If the abstract is accepted, a report and PPT presentation will be prepared.

Reservoir Simulation

The flow simulation work will continue to focus on CO_2 safe storage issues. Two simulation models: fault leakage model and cap rock fault model will be used to simulate the deep saline aquifer with leaking faults or the fractured cap seal rock during CO_2 injection. Chemical reactions will be added to the simulation to model CO_2 precipitation.

Cost and Milestone Status

Baseline Costs Compared to Actual Incurred Costs

2009 Oct 1 – Dec 31	Plan	Costs	Difference Plan minus Costs
Federal	$25,000	$28,490	($3,490)
Non-Federal	$9,410	$0	$9,410
Total	$34,910	$28,490	$6,410

Forecasted cash needs vs. actual incurred costs

Notes:

1. Federal plan amount based on original award of $400K averaged over 12 reporting quarters.
2. Cost this period reflects 3 months salary for J. Zeng and P. Geng, and 3 month for H. King
3. Non-Federal plan amount based on original budget cost share of $150,573 averaged as above.

Actual Progress Compared to Milestones

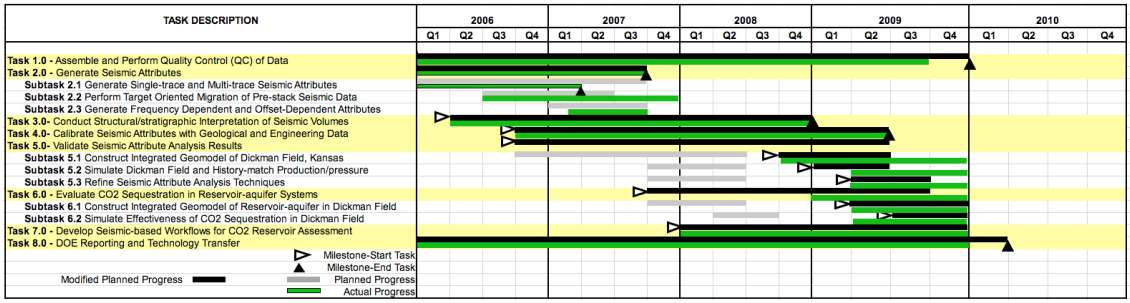

Summary of Significant Events

Problems and Significant Events

No problems to report.

As indicated in the Gantt chart above, we plan to request a 3 month no-cost extension of this project to 3/31/2010 to allow continued payment of Dr. June Zeng during the final report writing period.

PI C. Liner attended the AGU meeting in San Francisco (Dec. 2009) to attend CO_2 sequestration sessions. This trip was paid from non-project funds.

Two new MS students will be working on the Dickman data, but will not be funded out of the project. Bryan Flynn will do detailed mapping of the Mississippian unconformity and formation, including structure mapping (time and depth), fracture indication analysis, and porosity estimation. Shannon LeBlanc will shadow Bryan work but at the deeper Osage section of the Mississippian.

Continuing Personnel

Prof. Christopher Liner is Principle Investigator and lead geophysicist. He is a member of the SEG CO_2 Committee, Associate Director of the Allied Geophysical Lab, and has been selected to deliver the 2012 SEG Distinguished Instructor Short Course.

Dr. Jianjun (June) Zeng has been working exclusively on this project since Dec 2007 and is lead geologist. She will be funded through the end of 2009.

Heather King is a graduate MS student in geophysics who joined the project in January 2009 as a research assistant. She will be funded out of the project Jan-May and Sept-Dec 2009. She anticipates graduating in early 2010. Her thesis will focus on Ft. Scott to demonstrate the integrity of this formation as a seal for injected CO2. This will involve subtle structure and stratigraphy inferred by interpretation of multiple seismic attributes.

Dr. Po Geng has been working on this project as a specialist consultant since February, 2009. He will be funded out of the project, considered part-time, through the end of 2009.

Jintan Li is a graduate PhD student in geophysics who joined the project in Aug 2009. She is funded by Allied Geophysical lab at this time. Her thesis will be time-lapse seismic modeling (4D) for conducting dynamic reservoir characterization of the Dickman Field.

Technology Transfer Activities

A poster presentation entitled "Toward flow simulation for CO_2 sequestration at the Dickman oil field, Ness County, Kansas" was given at the 2009 SEG annual meeting in Houston.

Contributors

Christopher Liner (P.I, Geophysics)
Jianjun (June) Zeng (Geology and Petrel Modeling)
Po Geng (Flow Simulation)
Heather King (Geology and Geophysics, MS Candidate)
Jintan Li (Geology and Geophysics, Ph.D Candidate)

Tables

Table 1: CO2 trapping efficiencies at the end of the simulation (t=250 years) and the maximum bottom hole pressures

	STI	RTI	TEI	Maximum bottom hole Pressure (psia)
Vertical well CO_2 injection only	13%	40%	53%	2316
Horizontal well CO_2 injection only	17.4%	38.9%	56.3%	2149
Vertical well CO_2 and water injection	27.3%	30.7%	58.1%	5000
Horizontal well CO_2 and water injection	47.8%	46.5%	94.2%	2367

Table 2: Dickman Field General Reservoir Properties

Acreage = 240 acres
Net Pay Zone Thickness = 7 feet
Average depth = 4424 feet in MD
Oil API gravity γ_o = 37 API (0.84 g/cm^3)
The reservoir Temperature = 113 ^{o}F
The reservoir average pressure = 2066 psia
TDS (Total Dissolved Solid) salinity = 45,000 ppm
The aquifer water density $\gamma_w = 1.03\ \mathrm{g/cm^3}$ at reservoir condition
The reservoir water compressibility $C_w = 3 \times 10^{-6}\ 1/\mathrm{psi}$ at reservoir condition

Table 3: Simulation PVT Fluid Property Data Generated by Correlations

Pressure (psi)	Rs(ft^3/bbl)	B_o	Eg(ft^3/bbl)	viso(cp)	visg(cp)	C_o(1/psi)
14.696	4.57702	1.02309	5.12253	2.88422	0.0116	3.00E-05
280.383	52.8084	1.04008	101.477	2.15763	0.011898	3.00E-05
546.07	112.162	1.06205	205.282	1.67858	0.012346	3.00E-05
811.757	177.663	1.08745	316.794	1.36841	0.012921	3.00E-05
1077.44	247.634	1.11569	435.66	1.15573	0.013629	3.00E-05
1343.13	321.176	1.14643	560.565	1.00207	0.014475	2.41E-05
1608.82	397.718	1.17944	689.016	0.886241	0.015457	1.91E-05
1874.5	476.863	1.21454	817.581	0.795935	0.01656	1.56E-05
2140.19	558.314	1.25158	942.646	0.723589	0.017756	1.32E-05
2405.88	641.843	1.29046	1061.26	0.66433	0.019013	1.13E-05
2671.57	727.265	1.33106	1171.6	0.614891	0.020297	9.88E-06
2937.25	814.431	1.3733	1272.9	0.573001	0.021583	8.73E-06
3202.94	903.215	1.41711	1365.17	0.537039	0.022851	7.81E-06
3468.63	993.51	1.46243	1448.93	0.505816	0.024086	7.04E-06
3734.31	1085.22	1.50919	1524.89	0.47844	0.025281	6.40E-06
4000	1178.27	1.55734	1593.86	0.454231	0.026432	5.85E-06
4200	1249.16	1.59447	1641.66	0.437772	0.027267	5.49E-06
4400	1320.74	1.63235	1686.28	0.422623	0.028077	5.17E-06
4600	1392.98	1.67095	1728.02	0.408631	0.028862	4.88E-06
4800	1465.86	1.71026	1767.16	0.395665	0.029622	4.62E-06
5000	1539.37	1.75027	1803.94	0.383613	0.030359	4.38E-06

Table 4: Dickman data provided by Grand Mesa Production Company

Well Name	Cum Oil (BBL)	Cum Water	Water Cut
Dickman 1	336,592	2573284	88.4
Dickman 2	183,803	666748	78.4
Dickman 3	213,595	294029	57.9
Dickman 6	59,906	1078186	94.7
Dickman A1	174,720	0	0
Elmore 1	74,710	317099	80.9
Humphrey 1	56,472	0	0
Humphrey 2	39,030	0	0
Humphrey 3	14,718	0	0
Humphrey 4-18	5,994	26209	81.4
Sargent 5	60,400	0	0
Tilley #1	160,568	2029096	92.7
Tilley #2	115,330	0	0
Tilley #5	24,844	65864	72.6
Total	1,520,682	7050515	82.3

Figures

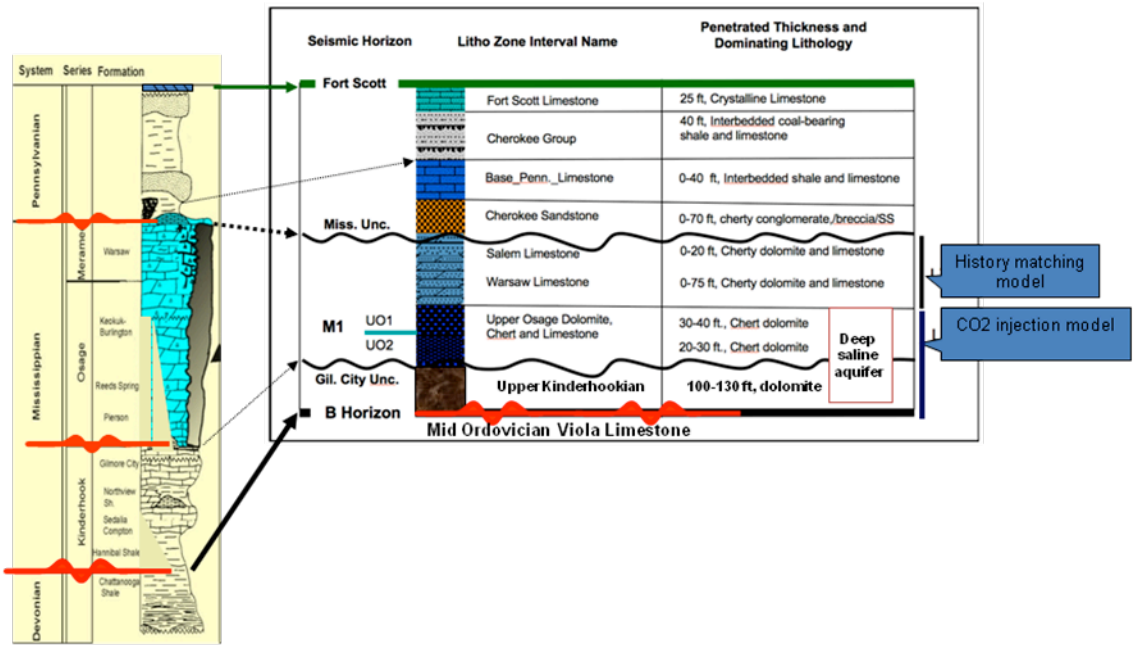

Figure 1: Target strata for history matching and CO2 injection simulation

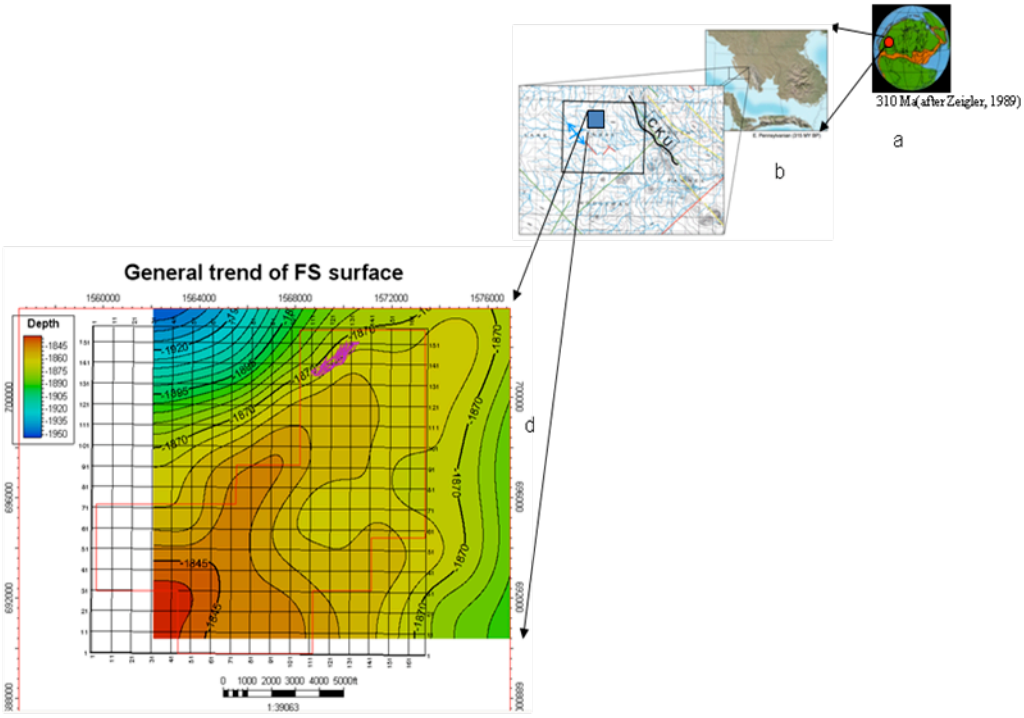

Figure 2: Regional and local structure maps (FS = Ft. Scott)

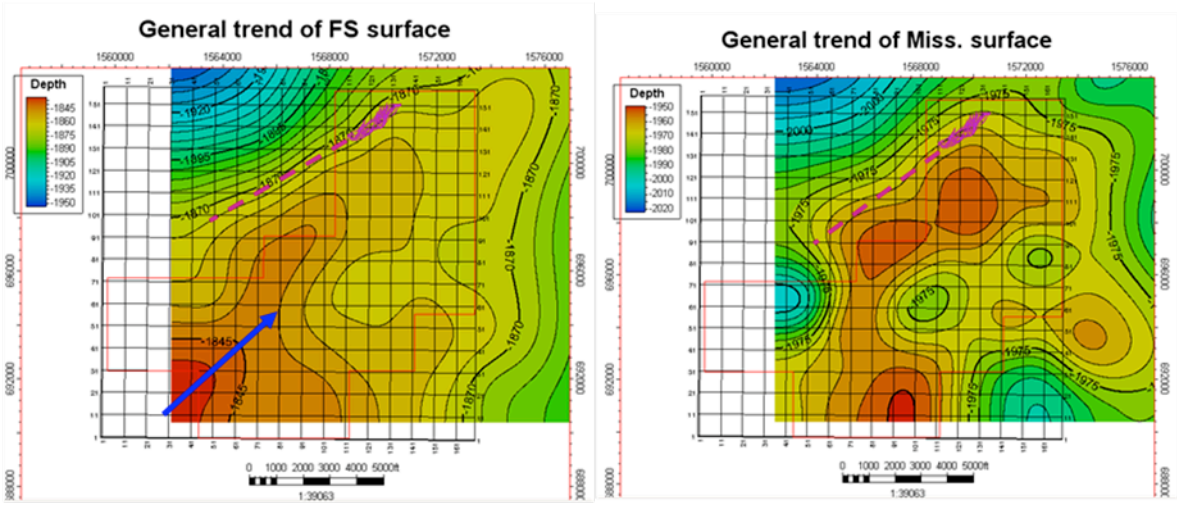

Figure 3: Formation top gridded depth maps for Pennsylvanian Ft. Scott and top Miss.

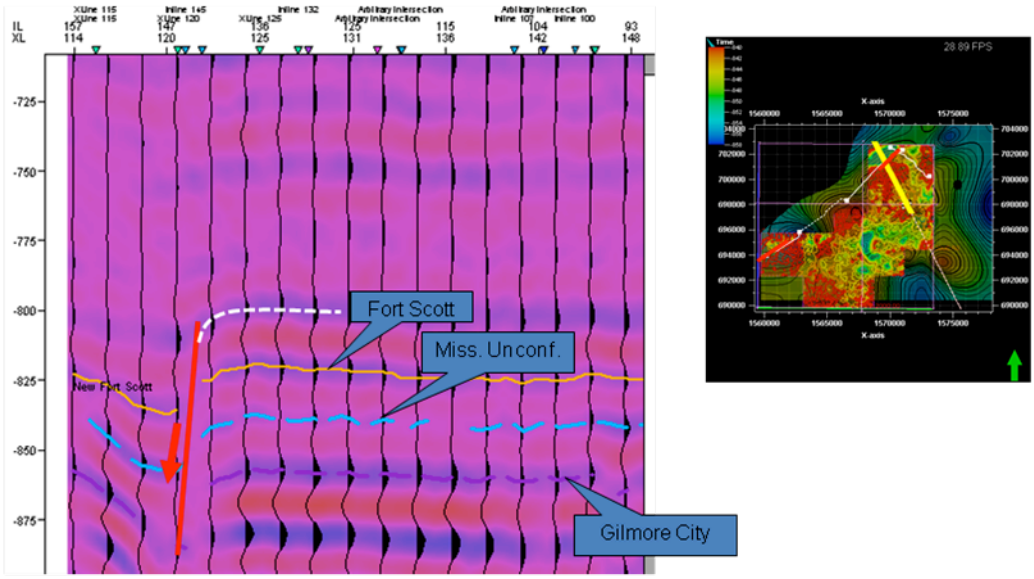

Figure 4: Seismic profile across the NE boundary fault

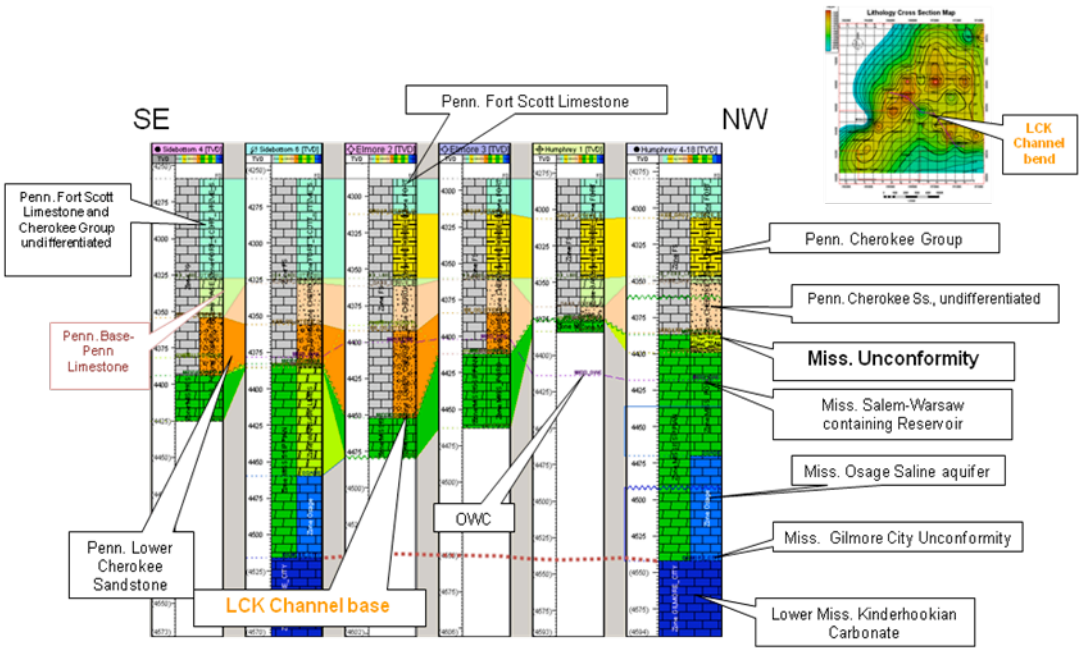

Figure 5: Cross section perpendicular to the structure

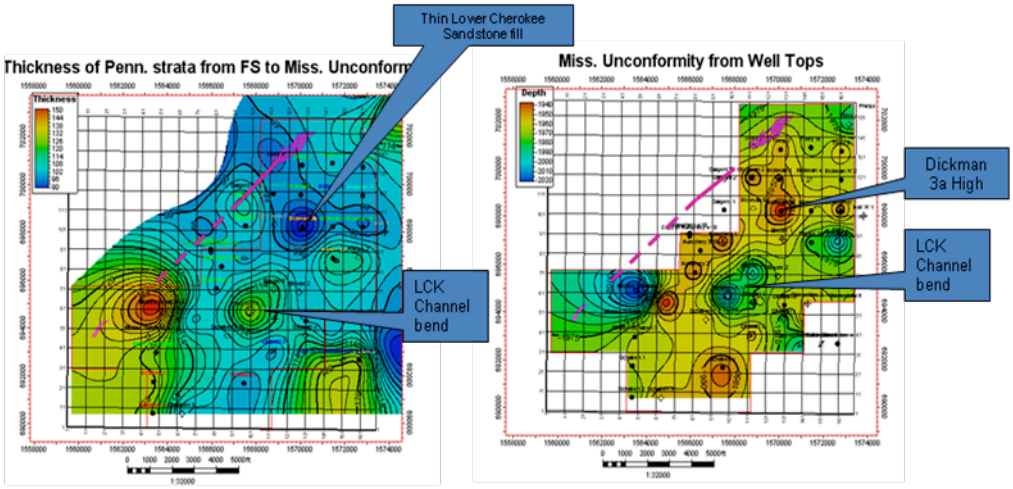

Figure 6: Thickness of Penn strata controlled by Miss paleotopography.

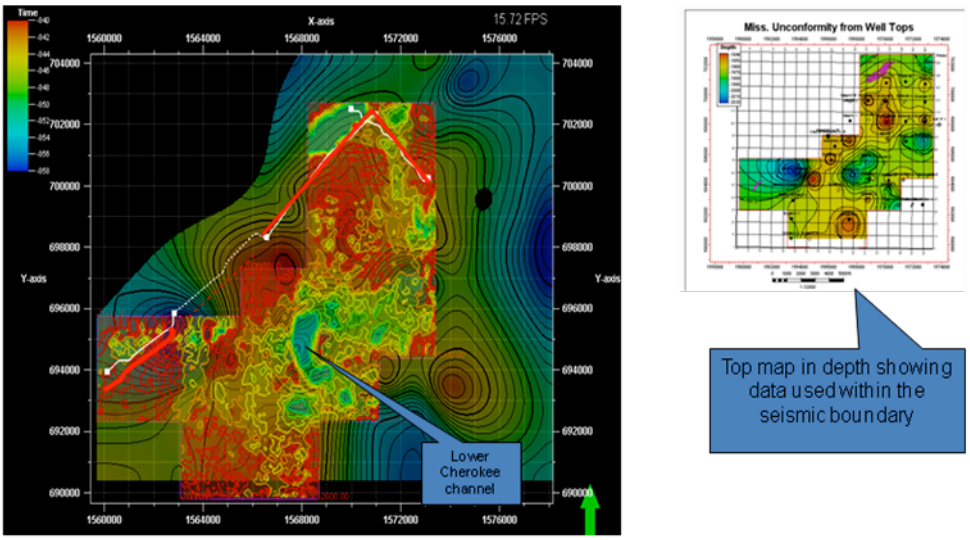

Figure 7: Overlay of seismic time structure and gridded formation top depth maps for the Miss unconformity.

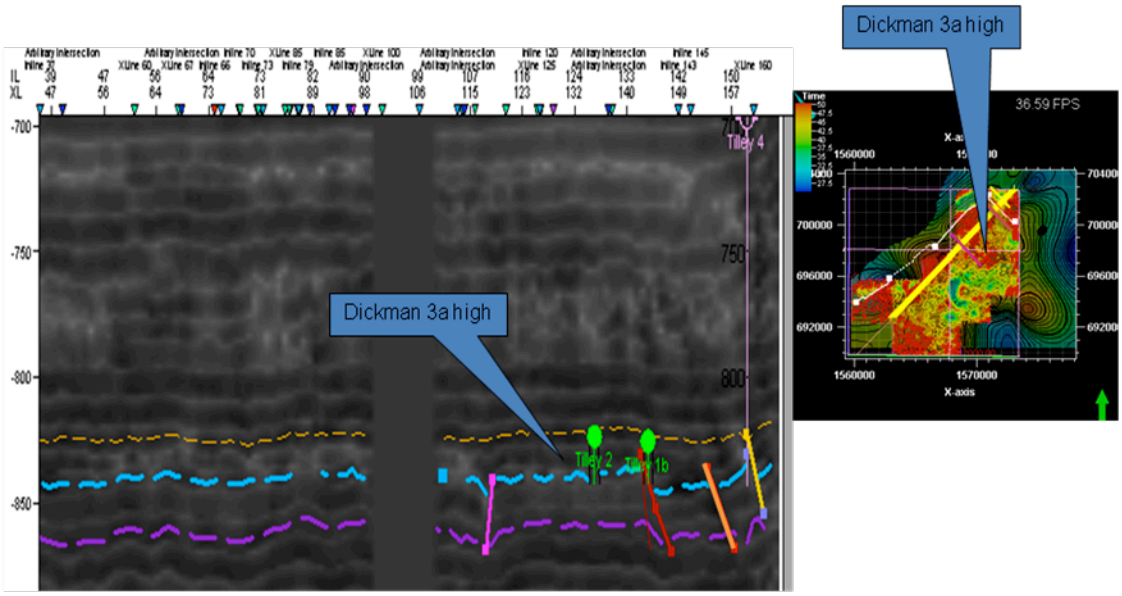

Figure 8: Seismic Spice profile parallel to the structure

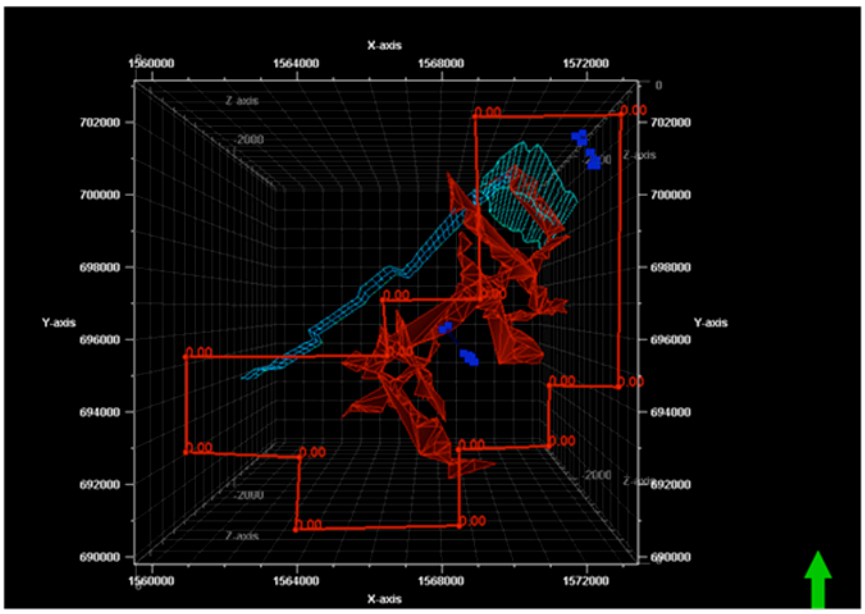

Figure 9: A fracture framework

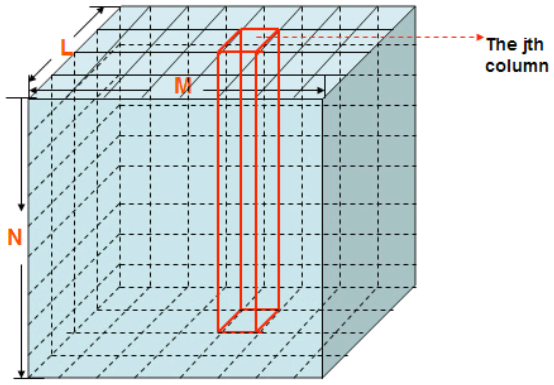

Figure 10: Flow Simulation 3D volume for export to 4D seismic workflow.

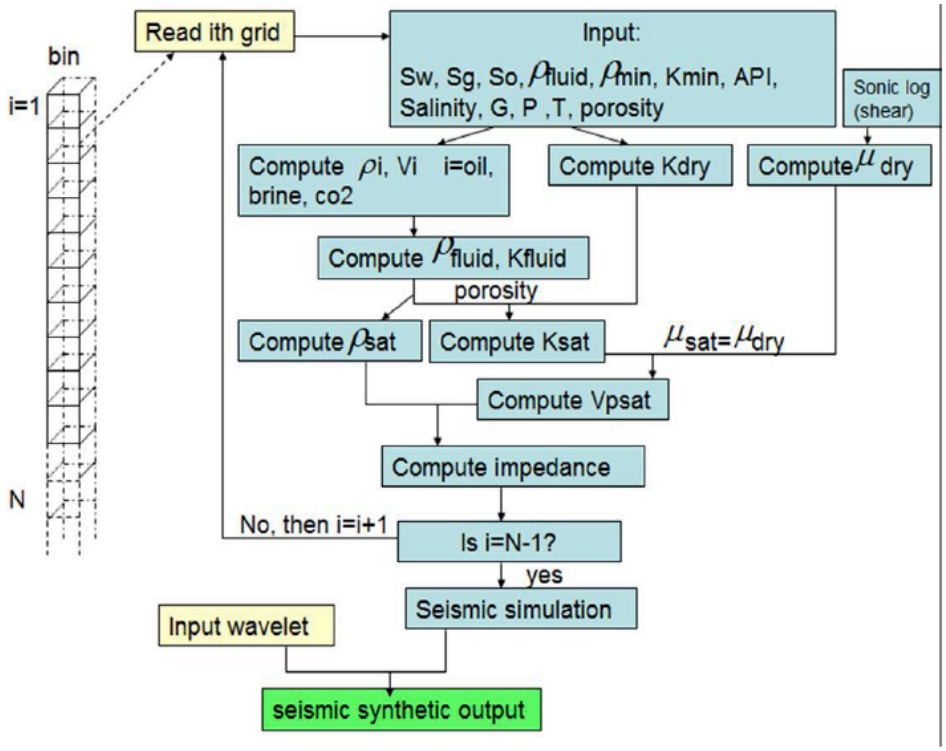

Figure 11: 4D seismic modeling work flow for one simulation column

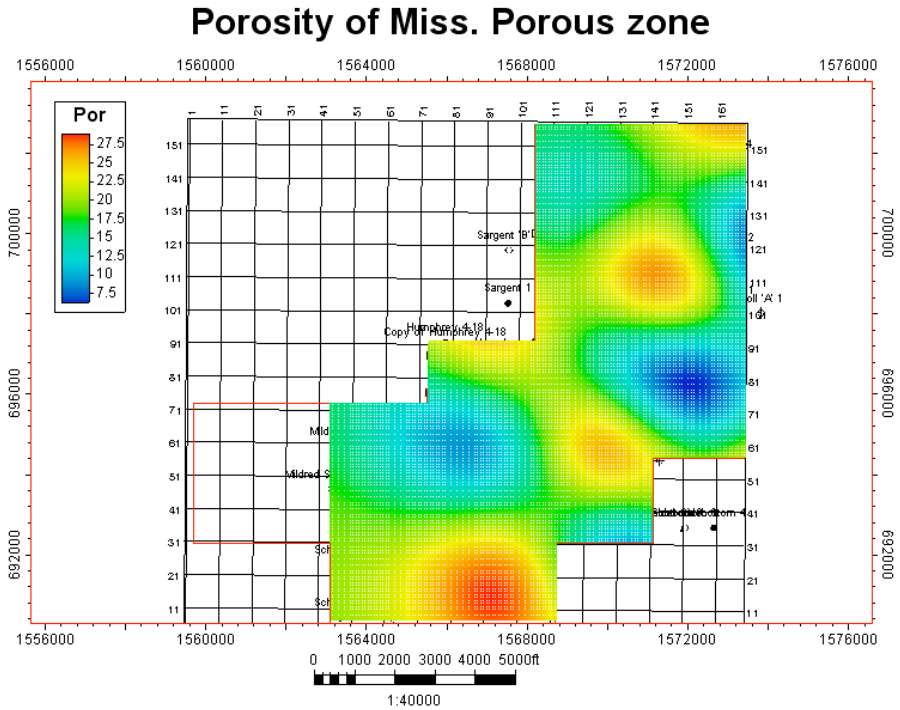

Figure 12: Porosity of Mississippian Porosity Zone used in 4D workflow.

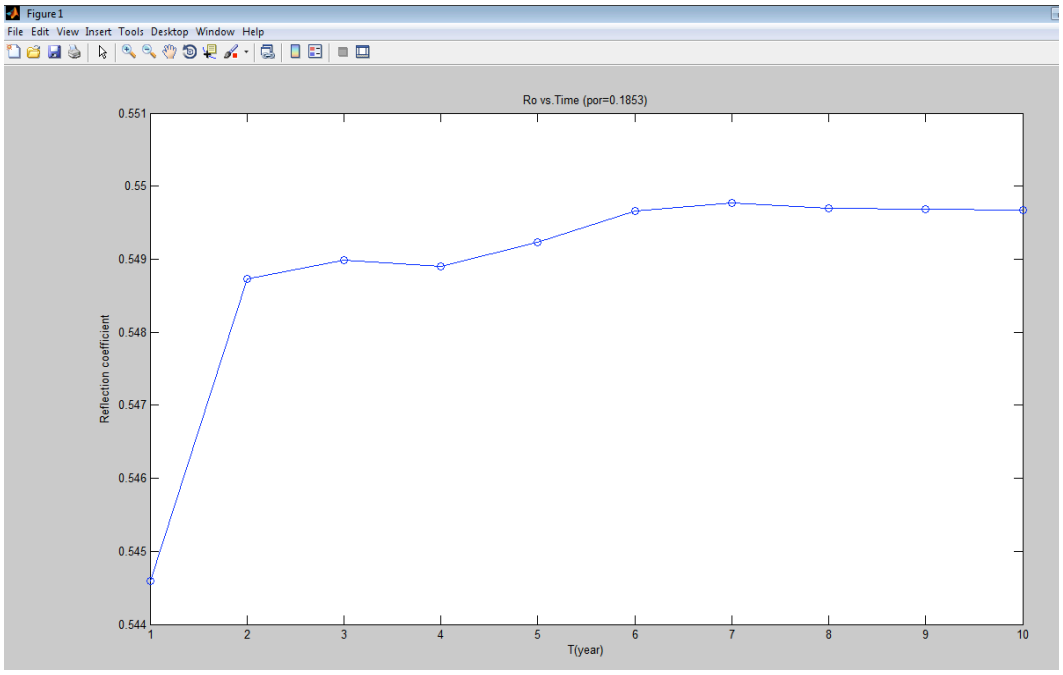

Figure 13: Example 4D reflection coefficient as a function of time (CO_2 saturation changes with temp, porosity = 0.1853)

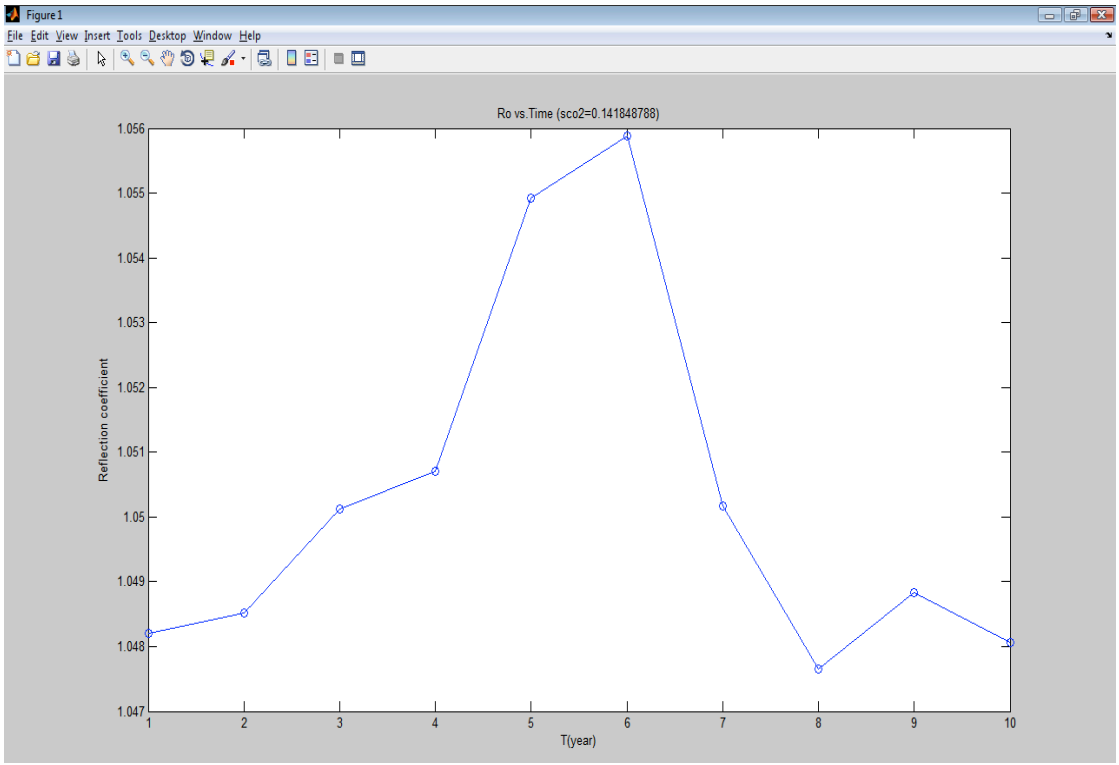

Figure 14: Example 4D reflection coefficient as a function of time (Porosity changes with time, S_{co2} =0.142)

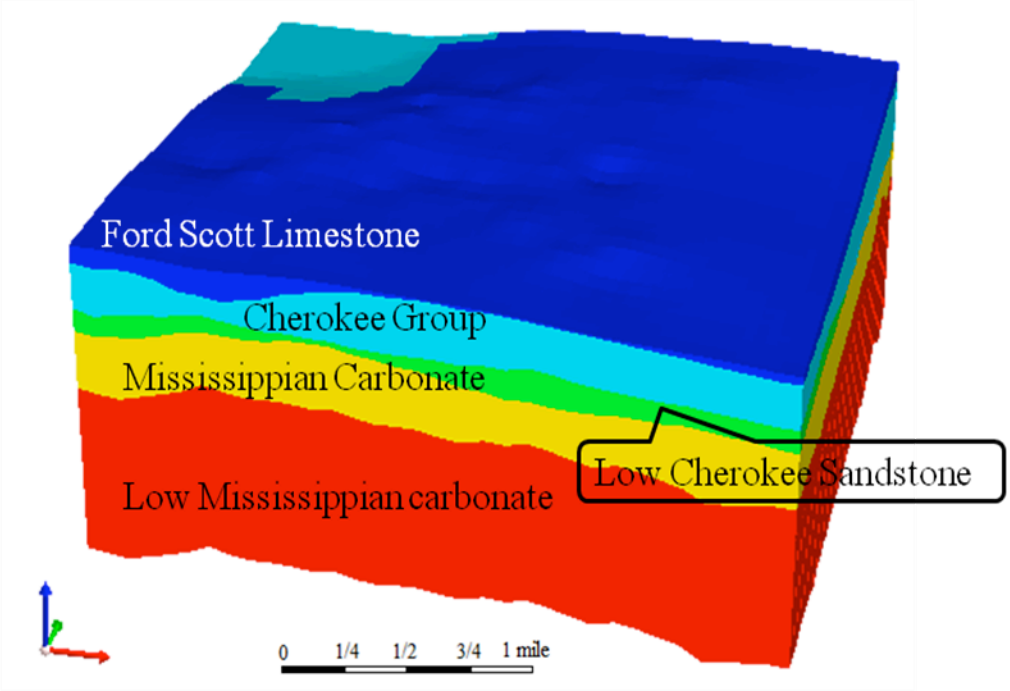

Figure 15: Five layer aquifer model for flow simulation

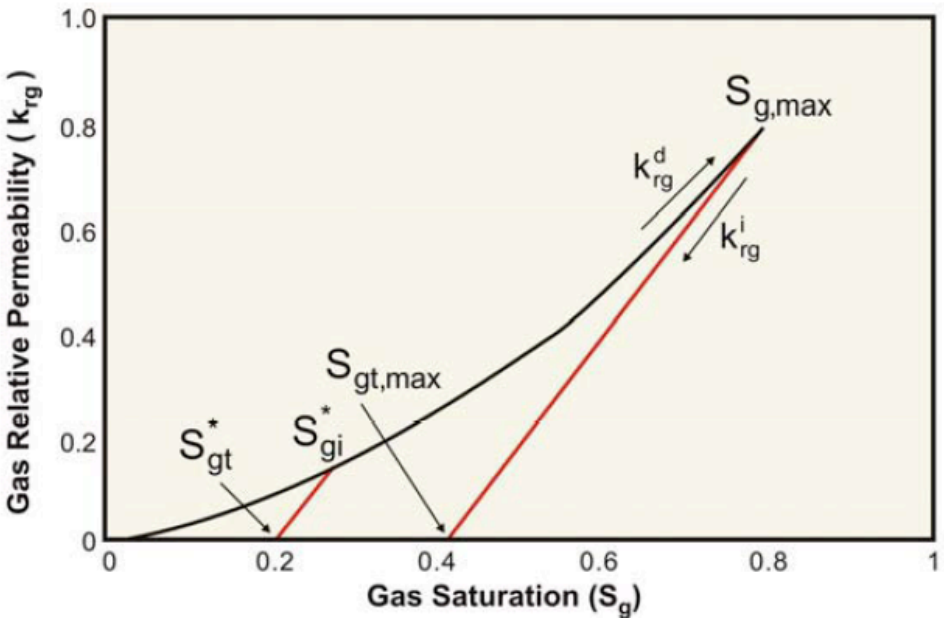

Figure 16: Land's Residual Trapping Model (Nghiem et al., 2009)

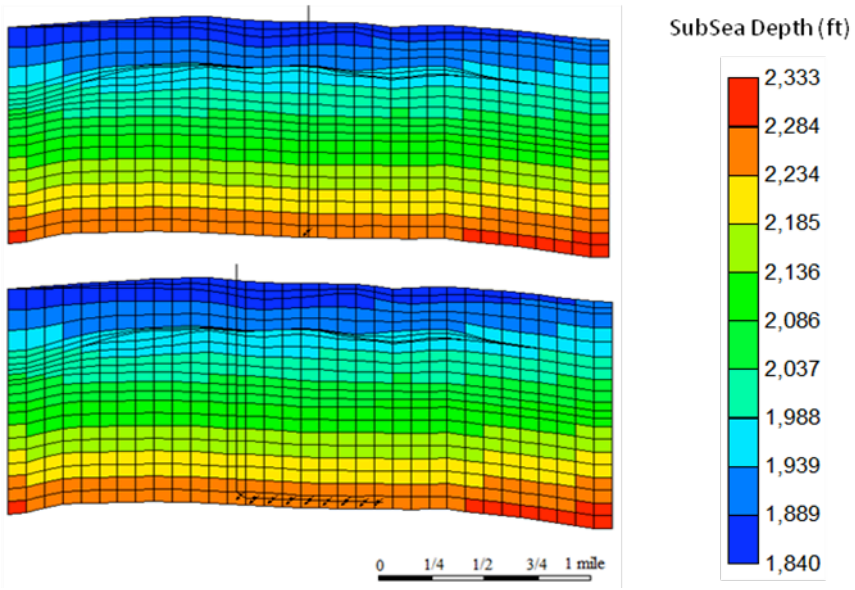

Figure 17: Vertical and horizontal CO_2 injecting well arrangements (Both injecting wells are perforated at the bottom layers).

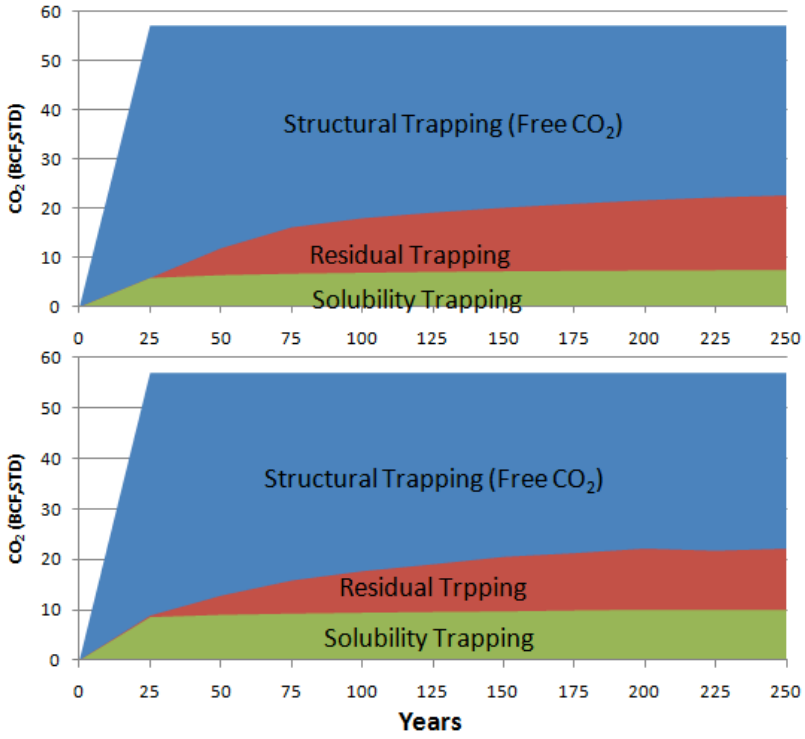

Figure 18: Comparison of the amount of CO_2 trapped by the vertical injection well(upper) and the horizontal injection well (lower). For CO_2 only injection, the horizontal injection can increase the solubility of CO_2 from 8% to 10%. There is no change in CO_2 residual gas trapping.

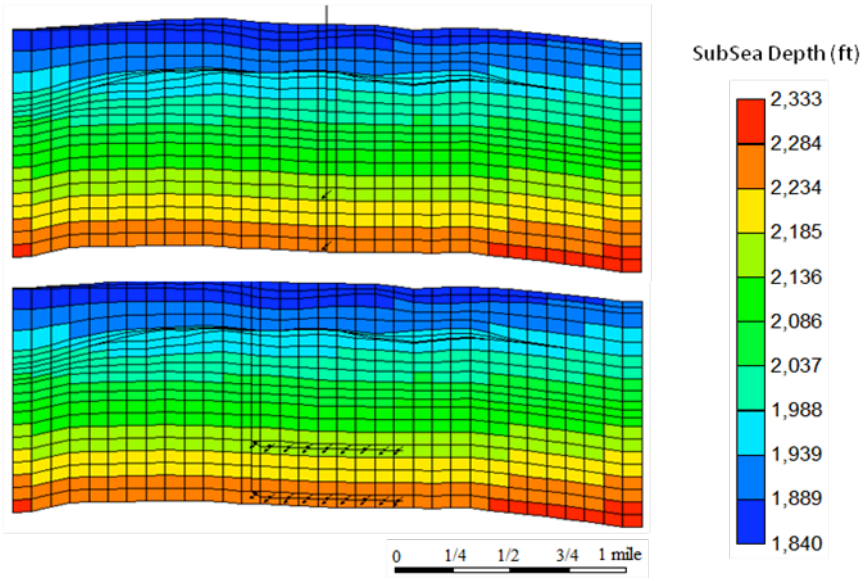

Figure 19: Vertical and horizontal CO_2 and brine water injection well arrangement (The brine water injection perforation is four layers above CO_2 bottom Perforation).

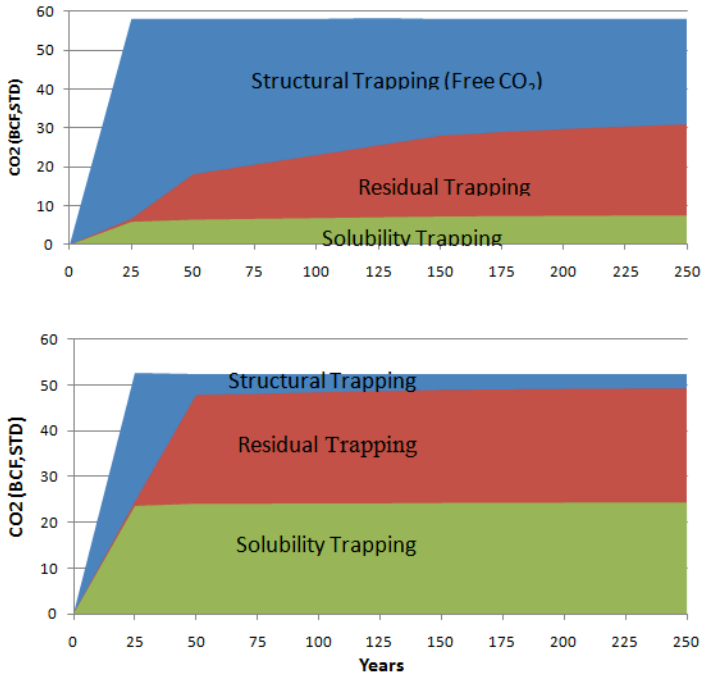

Figure 20: Comparison of amount of CO_2 trapped by the vertical injection well (upper) and the horizontal injection well (below) for CO_2 injection with water, the horizontal well can increase the trapping efficiency from 56% to 94%

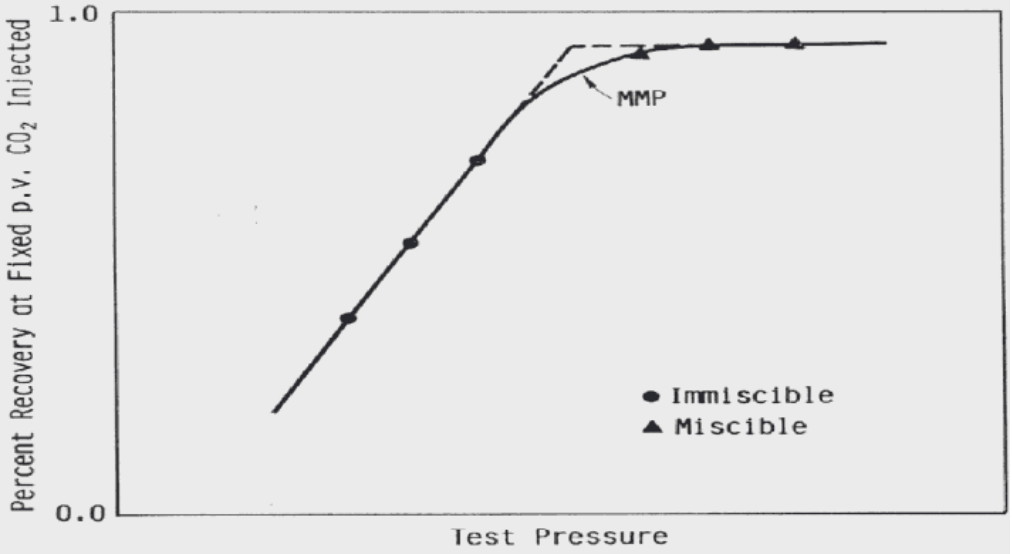

Figure 21: At MMP, the recovery vs. pressure curve experiences a sharp change in slope and levels off.

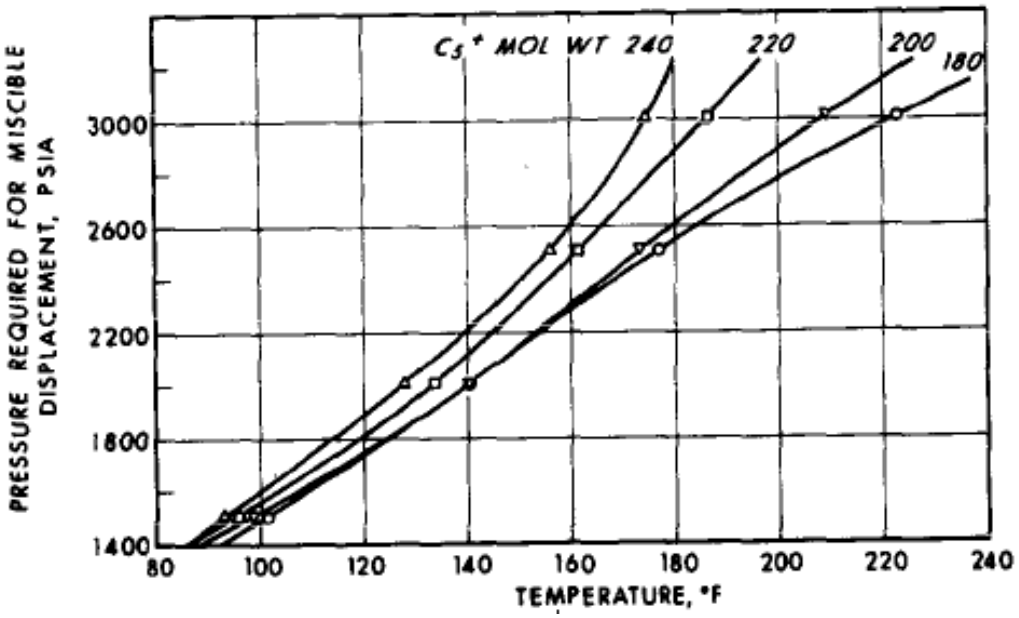

Figure 22: Correlation of predicting MMP for CO_2 flooding (Helm et al., 1974)

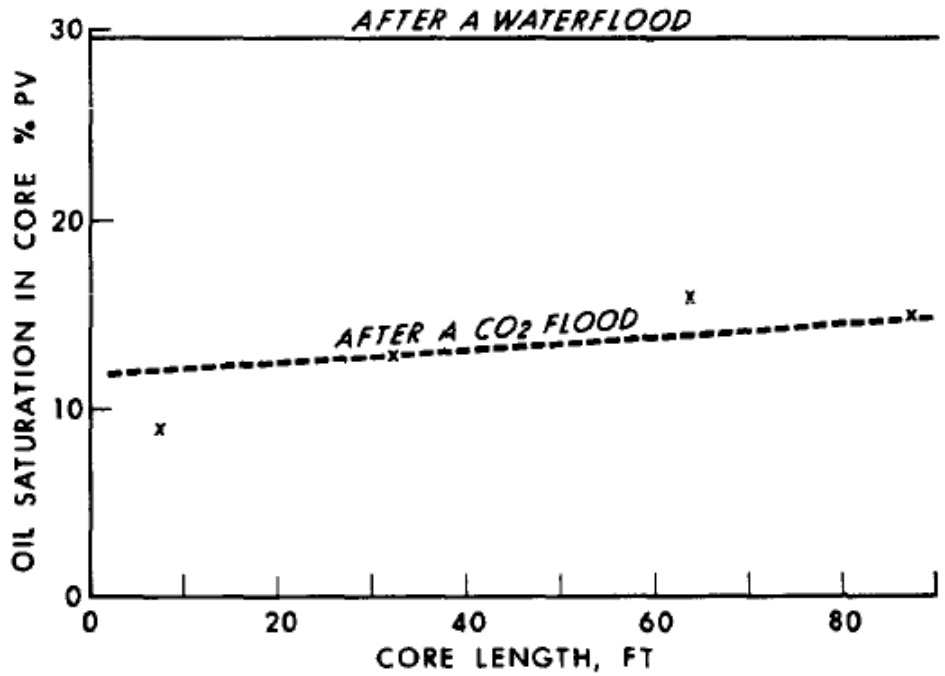

Figure 23: Comparison of Residual oil saturation after water flooding and immiscible CO2 flooding (at 900 psig and 75° F)

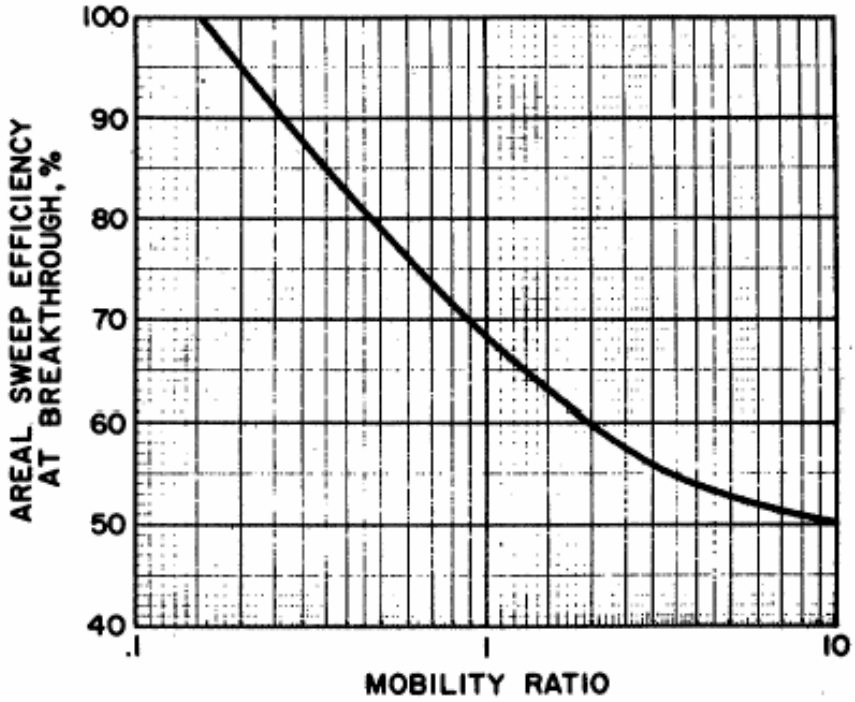

Figure 24: Correlation of areal sweep efficiency as a function of the water-oil mobility ratio for five-spot patterns (Craig, F. F. Jr. 1971)

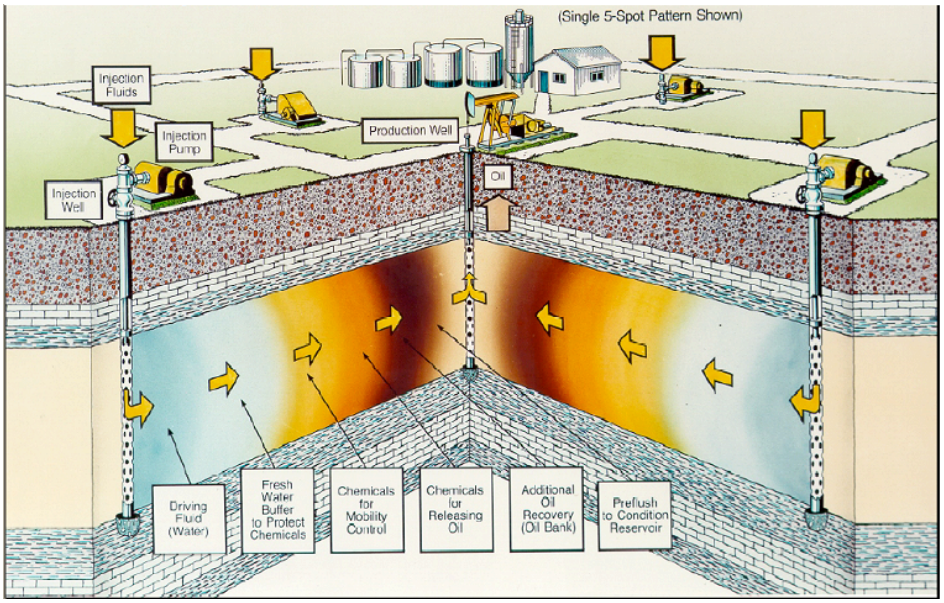

Figure 25: The general procedure of enhanced oil recovery with different chemical fluids.

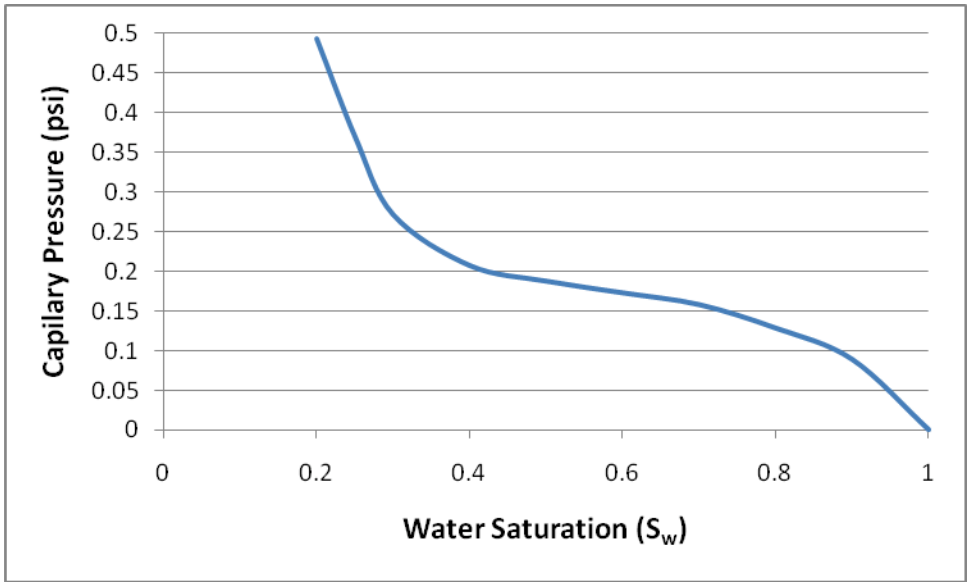

Figure 26: Capillary pressure cure for history matching in Mississippian carbonate zone

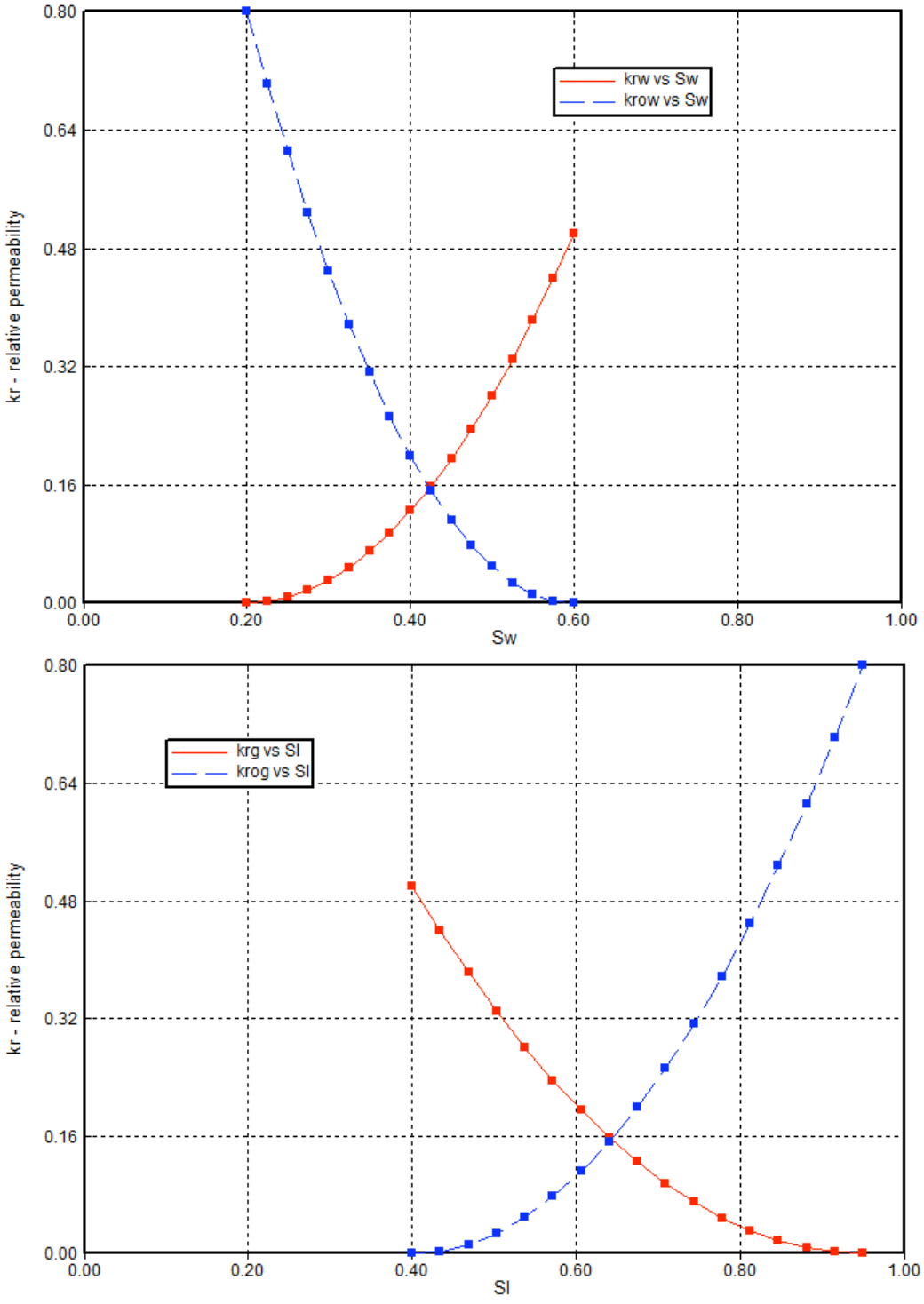

Figure 27: The water and oil relative permeability curves (Upper) and the gas and total liquid relative permeability curves (below) used in the simulation.

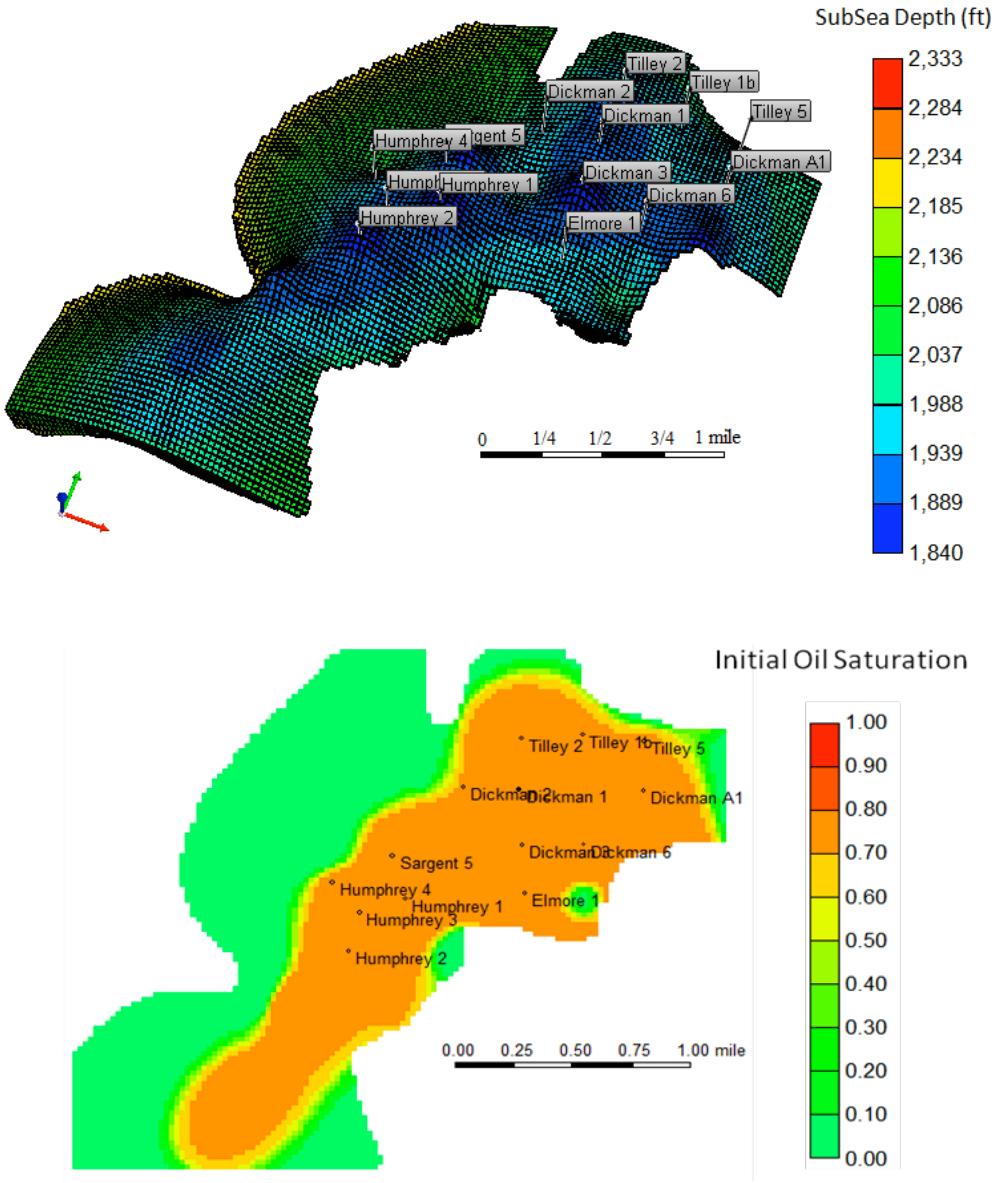

Figure 28: History match simulation grid model with 13 production wells (upper) and initial oil distribution with capillary transition zone (below)

References

Batzle, M., and Z. Wang, 1992, Seismic properties of pore fluids; Geophysics. 57, 1396-1408.

Carr, T. R., D. F. Merriam, and J. D. Bartley, 2005, Use of relational databases to evaluate regional petroleum accumulation, groundwater flow, and CO_2 sequestration in Kansas, AAPG Bulletin, 89, 12, 1607–1627.

Craig, F. F. Jr., 1971, The Reservoir Engineering Aspect of Water Flooding, SPE Monograph, Vol. 3.

Enick, R. M., Holder, R. M. and Morsi, B. I., 1988, A Thermodynamic Correlation for the Minimum Miscibility Pressure in CO_2 Flooding of Petroleum Reservoirs, SPE 14518.

Han, J., Carey, J. W., and Zhang, J., 2009, (2009), A coupled water chemistry and corrosion model for high salinity-high CO2 environments with application to wellbore integrity in CO2 sequestration:, *Eos Trans. AGU, 90(52)*, Fall Meet. Suppl., Abstract H11J-04

Helm, L. W. and Josendal, V. A., 1974, Mechanisms of Oil Displacement By Carbon Dioxide, SPE 4736.

Masalmeh, S.K., Abu-Shiekan, I. and Jing, X.D., 2005, Improved Characterization and Modeling of Capillary Transition Zones in Carbonate Reservoirs, IPTC 10238.

McCain, W.D. Jr., 1991, Reservoir-Fluid Property Correlations – State of the Art, SPERE, May, pp. 266-272.

Nghiem, L., C. Yang, V. Shrivatava, B. Kohse, M. Hassam, D. Chen and C. Card, 2009, Optimization of Residual Gas and Solubility Trapping for CO2 Storage in Saline Aquifer, SPE 119080.

Pedersen, K.S., Fredenslund, A. and Thomassen, 1989, **Properties of Oils and Natural Gases**, Gulf Publishing Company, p99-112.

Osif, T. L., 1988, The Effects of Salt, Gas, Temperature, and Pressure on the Compressibility of Water, SPE 13174.